# MINRob: A Large Force-Outputting Miniature Robot Based on a Triple-Magnet System

Yuxuan Xiang, *Graduate Student Member, IEEE*, Ruomao Liu, *Student Member, IEEE*, Zihan Wei, *Student Member, IEEE*, Xinliang Wang, *Student Member, IEEE*, Weida Kang, Min Wang, *Graduate Student Member, IEEE*, Jun Liu, *Member, IEEE*, Xudong Liang, and Jiachen Zhang, *Member, IEEE*

***Abstract*—Magnetically actuated miniature robots are limited in their mechanical outputting capability, because the magnetic forces decrease significantly with decreasing robot size and increasing actuating distance. Hence, the output force of these robots can hardly meet the demand for specific biomedical applications (e.g., tissue penetration). This article proposes a tetherless magnetic impact needle robot (MINRob) based on a triple-magnet system with reversible and repeatable magnetic collisions to overcome this constraint on output force. The working procedure of the proposed system is divided into several states, and a mathematical model is developed to predict and optimize the force output. These force values in magnetic impact and penetration are obtained from a customized setup, indicating a ten-fold increase compared with existing miniature robots that only utilize magnetic attractive force. Eventually, the proposed MINRob is integrated with a teleoperation system, enabling remote and precise control of the robot's position and orientation. The triple-magnet system offers promising locomotion patterns and penetration capacity via the notably increased force output, showing great potential in robot-assisted tissue penetration in minimally invasive healthcare.**

***Index Terms*—Magnetic collision, magnetic force, magnetic miniature robots, tissue penetration, triple-magnet system.**

Manuscript received 17 December 2023; revised 17 April 2024; accepted 6 May 2024. Date of publication 5 June 2024; date of current version 19 June 2024. This paper was recommended for publication by Associate Editor P. Renaud and Editor M. Yim upon evaluation of the reviewers' comments. This work was supported in part by the National Natural Science Foundation of China under Grant 62303387 and Grant 12322207, and in part by the Research Grants Council of the Hong Kong Special Administrative Region, China under Grant CityU21202822. The work of Xudong Liang and Weida Kang were supported in part by the Fundamental Research Funds for the Central Universities under Grant HIT. OCEF. 2022037 and in part by the Science Technology and Innovation Program of Shenzhen under Grant JCYJ20220531095210022. *(Corresponding authors: Jiachen Zhang; Xudong Liang.)*

Yuxuan Xiang, Ruomao Liu, Zihan Wei, Xinliang Wang, and Jiachen Zhang are with the Department of Biomedical Engineering, City University of Hong Kong, Hong Kong, SAR, China (e-mail: yxxiang.bme@my.cityu.edu.hk; ruomaoliu2-c@my.cityu.edu.hk; zihanwei3-c@my.cityu.edu.hk; xlwang.bme@my.cityu.edu.hk; jzhang.bme@cityu.edu.hk).

Weida Kang and Xudong Liang are with the School of Science, Harbin Institute of Technology, Shenzhen 518172, China (e-mail: kangweida@stu.hit.edu.cn; liangxudong@hit.edu.cn).

Min Wang and Jun Liu are with the Department of Mechanical Engineering, City University of Hong Kong, Hong Kong, SAR, China (e-mail: min.wang@my.cityu.edu.hk; jliu287@cityu.edu.hk).

This article has supplementary downloadable material available at https://doi.org/10.1109/TRO.2024.3410096, provided by the authors.

Digital Object Identifier 10.1109/TRO.2024.3410096

## I. Introduction

MAGNETIC small-scale robots exhibit significant potentials to be employed in demanding scenarios in biomedical applications [1], [2], [3] with various functionalities [4], [5], [6], [7]. These robots can achieve noninvasive access and remote navigation in hard-to-reach regions buried deep inside human bodies (e.g., gastrointestinal tract [8], [9], [10] and blood vessel [11], [12], [13]). To attain these functionalities, magnetic field actuators induce magnetic force and torque to the robot body, which functions as an end-effector to conduct desired tasks. However, demanding real-world biomedical functionalities (e.g., long-lasting anchoring and tissue penetration) can hardly be accomplished, attributed to insufficient force and torque output [14]. The values of output forces and torques decrease significantly with decreasing robot size and increasing actuating distance.

Previous studies have demonstrated various tailored robot structures to enhance the mechanical output [15], [16]. However, these designs fail to essentially increase the magnetic interaction force. Considering the restrictions of present peripherals, pure magnetic pulling force and torque exerted on small-scale robots rarely fulfill the requirements of targeted mechanical operations in real-world biomedical applications (e.g., tissue penetration and removal) [14]. Researchers generate potentially larger force and torque output via extra energy to resolve these challenges. For example, elastic potential energy prestored through deformable elastomers has been adopted with unique elastic properties [17] and spring structures [18]. Nevertheless, an additional energy source is often required to trigger the energy release. In the meantime, such predeformed structures are one-offs and not applicable for continuous outputs and operations sustained over a long time.

On the other hand, kinetic energy resulting from pulse-induced momentum offers an alternative solution to generate instantaneous and enormous magnetic force. This approach has been applied to a millirobot composed of a free-to-move spherical magnet inside a hollow tubular shell [19], where the magnetic pulse generated by a pair of electromagnetic coils actuates the spherical magnet to accelerate along the tube. The momentary impact amplifies the force when the high-speed sphere hits the rigid plate on the anterior side. The direction of the magnetic pulse is switched with a frequency up to several hertz

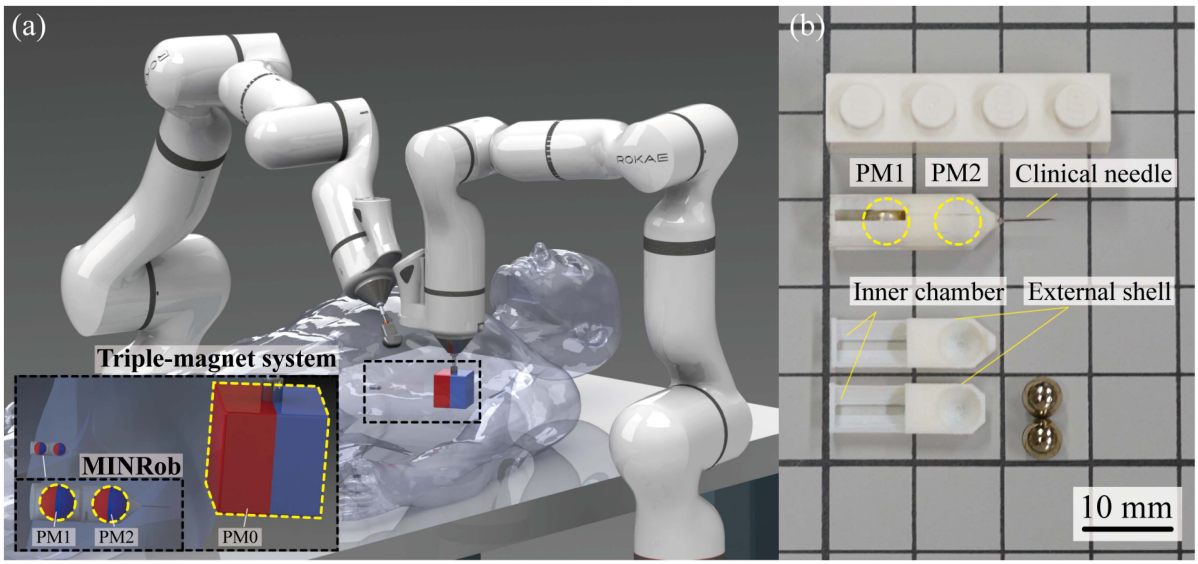


Fig. 1. Proposed small-scale robotic system. (a) A schematic showing the teleoperated robot with its triple-magnet system to be potentially deployed inside a human body for minimally invasive diagnostic or therapeutic applications. The magnetic robot, composed of two spherical magnets (PM1 and PM2), is capable of navigating and anchoring inside the human body, for which the external actuating magnet (PM0) and ultrasound probe are attached to the robotic arms to provide programmable control and real-time imaging, respectively. (b) A photograph of the MINRob. The robot is composed of PM1, PM2, an external shell, and a clinical needle.

to accomplish reversible forward and backward locomotion of the sphere. In addition, magnetic impact systems with two [20], [21] and three degree-of-freedoms (DOFs) [22] have been developed to extend the locomotion of the robots, enabling them to navigate in unstructured environments, such as interior cavities, ducts, and vessels of the human body. Although such collisions between magnetic parts and nonmagnetic parts are reversible, the pulse-based impact demands a significantly high frequency with substantial energy density. Meanwhile, a spacious gap is required to fully accelerate the robot before impact, which is incompatible with the inherently limited onboard space of small-scale robots.

The magnetic field-induced collision between multiple magnetic parts is demonstrated to increase energy intensity in limited space. It is commonly observed in nuclear physics at the microlevel [23]. Examples include the chiral magnetic effect for the heavy-ion collision [24]. Nonetheless, there are few applications of collision between multiple magnetized components at the macrolevel. A Gauss gun triggered by a magnetic resonance imaging (MRI) scanner can induce collisions between spherical permanent magnets and steel spheres [25]. Apart from the global force externally applied by the magnetic field, the additional local attractive force increases significantly as one magnetized component approaches another. Such momentum-induced inelastic collisions propagate along the approaching direction to the robot body. However, the firing of the Gauss gun is disposable and irreversible due to the immense attractive force of magnetic coupling, failing to meet the requirements for continuous and repeated operations in biomedical applications [26].

Meanwhile, the aforementioned designs are confined by the field generators in surgical environments, such as electromagnetic coil systems and clinical MRI scanners. These electromagnetic coil systems also require preprogrammed signals and bulky cooling modules to accomplish sophisticated and high-frequency switching. Furthermore, commercial sintered permanent magnets (e.g., NdFeB) are extremely brittle materials with high operational risk, and thus magnetic collision can damage materials and cause physical injury during operations.

To overcome the aforementioned limitations, this article proposes a magnetic impact needle robot (MINRob) capable of reversible magnetic collision actuated by a rotating cubic permanent magnet via a teleoperation robotic system, as illustrated in Fig. 1(a). Inside the proposed MINRob, the active spherical magnet is free to rotate and translate, while the passive spherical magnet is free to rotate. Combined with the actuating cubic magnet outside the millirobot, we present a triple-magnet system, which is able to achieve repeatable collision at various speeds, leading to a notably larger force output from the proposed millirobot compared with preceding studies. We reversibly achieve the macroscale magnetic collision for the first time and integrate the robotic system with a computer-aided teleoperation platform. We also develop a mathematical framework to model the triple-magnet system's magnetic force and torque interactions, understand the prerequisites of unlocking the magnetic chaining state, and optimize the system's mechanical performance. We experimentally measure the angle variations of each magnetic component via a high-speed camera. The obtained real-time angle data, together with results from the finite element analysis (FEA), validate the accuracy and reliability of our model. Finally, we present the locomotion of MINRob based on the triple-magnet system while demonstrating its penetration performance with a multilayer film in a tube and a soft matrix in an unconstrained 3-D environment.

Considering the real-world biomedical applications, the proposed triple-magnet system enables remote control on the access in the deep layer of muscle of the patient, which still

poses a great challenge for conventional surgery. Our MINRob is able to provide a large outputting force for a long-lasting operation. Integrating with specific functional units, it is potentially capable of tissue penetration, implant therapy, and drug delivery.

The rest of this article is organized as follows. The structural design of the proposed robot and its working principle are briefly introduced in Section II. In Section III, we present the mathematical model of the triple-magnet system in various states. Section IV conducts numerical simulations to optimize the impact force while the variables of the triple-magnet system are determined. In Section V, critical parameters involved in the proposed model are characterized through experiments. In Section VI, we provide demonstrations to evaluate the performance of the triple-magnet system. We further discuss more factors affecting the robot's performance, force comparison, and potential applications in Section VII. Finally, Section VIII concludes this article.

## II. Actuation Principle

Here, we denote the actuating cubic permanent magnet outside the robot, the active spherical magnet inside the robot, and the passive spherical magnet inside the robot as permanent magnet 0 (PM0), permanent magnet 1 (PM1), and permanent magnet 2 (PM2), respectively, see Fig. 1(a). To characterize the proposed triple-magnet system, we introduce the MINRob as the container to achieve the desired locomotion of PM1 and PM2. As shown in Fig. 1(b), MINRob is composed of two spherical magnets (PM1 and PM2), an external shell, and a clinical needle. The external shell is fabricated by polylactic acid (PLA) via 3-D printing (Raise3D Pro3 Plus), and the extra clinical needle (stainless steel, 25 G, Kindly Medical Inc.) is attached to the tip. The needle is able to utilize the induced large impact force for potential medical applications (e.g., tissue penetration), while minimizing the undesired swinging motion of the robot. The external shell is divided into two halves that can be glued together to position two spherical magnets inside. In this case, PM1 is free to rotate and translate within the inner chamber, while PM2 is only free to rotate. The external geometric structure of MINRob comprises a cone and a cylinder part, where a gap is fabricated on the sides to observe the position of PM1.

The structure of the MINRob constrains the locomotion of PM1 and PM2, and thus PM1 can only translate along the axial direction. If specific mechanical constraints are provided to the robot body, PM1 is able to achieve a periodic "bouncing-off" motion under the actuation of the rotating PM0 in an orientation illustrated in Fig. 1(a). Although PM0 continuously exerts attractive forces on both PM1 and PM2, an even larger repulsive force from PM2 to PM1 is achievable as they rotate synchronously with PM0. Therefore, this force keeps PM1 away from PM2 in the manner of a bouncing-off motion along the inner chamber of the MINRob. As PM0 continues to rotate, the attractive force dominates again, and thus PM1 hits back at a high speed, generating a corresponding large force in the axial direction. This circulation of impact is triggered repeatedly as the PM0 rotates.

The fundamental geometric variables involved in the triple-magnet system are mathematically modeled in Section III and optimized in Section IV. Eventually, the parameters are determined and listed in Table II.

## III. Mathematical Modeling

The mathematical model developed for the system in various states is applied for the $X$-$Y$ plane, as shown in Fig. 2. The corresponding magnetic moments of PM0, PM1, and PM2 are denoted as $\mathbf{m}_0 \in \mathbb{R}^{3\times1}$, $\mathbf{m}_1 \in \mathbb{R}^{3\times1}$, and $\mathbf{m}_2 \in \mathbb{R}^{3\times1}$. PM0 is the actuating magnetic component whose orientation, position, rotating frequency, and rotating direction are actively controlled. PM1 is free to rotate and translate within the inner chamber, while sphere PM2 can only rotate. The orientations of PM1 and PM2 are determined by PM0, of which the magnetic moment aligns with PM1 and PM2 at the initial aligning state and rotates to induce the magnetic chaining, bouncing-off, and hitting-back state (Fig. 2). An ideal orientation of the impact along the $X$-axis is discussed in this model. In real-world applications, the entire robot's body composed of PM1 and PM2 tends to rotate synchronously with PM0 if no supports are found to balance the torque in the $Z$-axis. To avoid the circumstance, a structural support is added to the robot body, as presented in the enlarged view in Fig. 2(a). The structural support can be achieved by preanchoring a small part of the needle or placing the robot in a hollow tube. Therefore, the orientation of the robot is controlled, although a small swing on the body is observed. This undesired swinging motion can be mitigated by decreasing the diameter of the hollow tube, increasing the insertion depth of the needle tip, or increasing the actuating distance of PM0. Due to the adjustable swing amplitude, we ignore the swinging motion of the robot's body and assume that MINRob is always vertical to the substrate in our model, as presented in Fig. 2(a)–(e).

In an ideal configuration, PM1 and PM2 rotate synchronously with the rotating PM0. As the rotation angle exceeds a threshold, the local magnetic attractive force between PM1 and PM2 converts into repulsive force, as presented in Fig. 2(c), which induces a "bouncing-off" motion of the free-to-translate sphere PM1. A significantly large impact force is induced when PM1 hits back.

Previous research has studied the interaction forces between two magnetic agents in a uniform external magnetic field [27], [28], [29]. Similarly, our model utilizes the magnetic dipole model to analyze the force and torque interactions of two magnetic agents (i.e., PM1 and PM2), but the discussion is under a nonuniform magnetic field with a gradient generated by PM0. To ensure the reliability of our calculation compared with real-world applications, the distances between each magnet are always larger than 3.5 radii of its minimum bounding sphere, which efficiently constrains the error of the dipole model to below 2% [30].

As shown in Fig. 3(a), a clockwise rotation of PM0 leads to counterclockwise rotations of both PM1 and PM2. Thus, we denote the rotating angle of PM0, PM1, and PM2 as $\theta_0 \in (-2\pi, 0]$, $\theta_1 \in [0, 2\pi)$,and $\theta_2 \in [0, 2\pi)$. For $i \in \{0, 1, 2\}$, we have

$$\mathbf{m}_i = [m_i \cos\theta_i, m_i \sin\theta_i, 0]^T \tag{1}$$

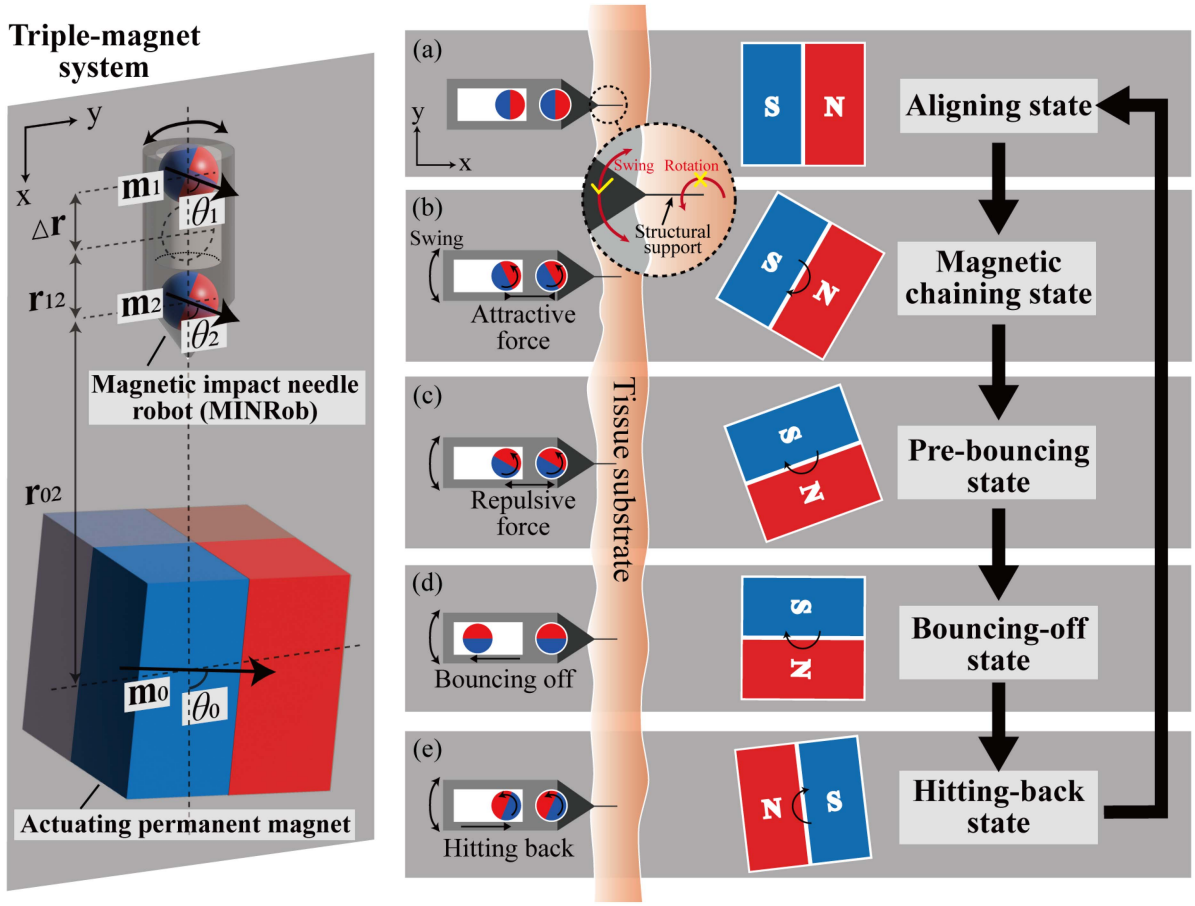


Fig. 2. Schematic illustrating the magnetic interactions and actuating process of the triple-magnet system with relevant variables defined in the developed mathematical model. The orientation and position of individual magnetic components are shown in various states, ranging from (a) to (e). A MINRob is illustrated to continually hit and insert into a tissue substrate under the actuation of an external rotating permanent magnet.

where $m_i$ is the numerical value of the corresponding magnetic dipole moment, and the distance vector between the magnetic dipole moment center of PM0 and PM2, PM1 and PM2 are denoted as $\mathbf{r}_{02} \in \mathbb{R}^{3\times1}$ and $\mathbf{r}_{12} \in \mathbb{R}^{3\times1}$, respectively. The magnetic flux density $\mathbf{B}_i$ at a point $\mathbf{P}_j \in \mathbb{R}^{3\times1}$ (for $j \in \{0,1,2\}$) generated by $\mathbf{m}_i$ at point $\mathbf{P}_i \in \mathbb{R}^{3\times1}$ is calculated as [31]

$$\mathbf{B}_i\left(\mathbf{P}_j\right) = \frac{\mu_0}{4\pi r_{ij}^3}(3\hat{\mathbf{r}}_{ij}\hat{\mathbf{r}}_{ij}^T - \mathbb{I}_3)\mathbf{m}_i \tag{2}$$

where $\mu_0 = 4\pi \times 10^{-7}$ H/m is the vacuum permeability, $\mathbf{r}_{ij}$ is the distance vector from $\mathbf{m}_i$ dipole center $\mathbf{P}_i$ to point $\mathbf{P}_j$, $\hat{\mathbf{r}}_{ij}$ is the unit vector in this direction, $r_{ij}$ is the distance length, and $\mathbb{I}_3$ is the $3 \times 3$ identity matrix. The magnetic force $\mathbf{F}_{ij} \in \mathbb{R}^{3\times1}$ and torque $\boldsymbol{\tau}_{ij} \in \mathbb{R}^{3\times1}$ of $\mathbf{m}_j$ at point $\mathbf{P}_j$ generated by $\mathbf{m}_i$ are calculated as

$$\begin{aligned}\mathbf{F}_{ij}(\mathbf{P}_j) = \frac{3\mu_0}{4\pi r_{ij}^4}((\hat{\mathbf{r}}_{ij}^T\mathbf{m}_i)\mathbf{m}_j + (\hat{\mathbf{r}}_{ij}^T\mathbf{m}_j)\mathbf{m}_i \\ + (\mathbf{m}_i^T\mathbf{m}_j - 5(\hat{\mathbf{r}}_{ij}^T\mathbf{m}_i)(\hat{\mathbf{r}}_{ij}^T\mathbf{m}_j))\hat{\mathbf{r}}_{ij})\end{aligned} \tag{3}$$

$$\boldsymbol{\tau}_{ij}\left(\mathbf{P}_j\right) = \mathbf{m}_j \times \mathbf{B}_i\left(\mathbf{P}_j\right). \tag{4}$$

### A. Aligning State

In the initial aligning state, the magnetic moment directions of PM0, PM1, and PM2 are aligned along the $X$-axis, as illustrated in Fig. 2(a). In this specific state, $\theta_1$ and $\theta_2$ can be calculated from (5) due to the torque equilibrium on PM1 and PM2 as PM0 rotates for a degree $\theta_0$.

$$\begin{cases}\boldsymbol{\tau}_{21}^z\left(\mathbf{P}_1\right) = -\boldsymbol{\tau}_{01}^z\left(\mathbf{P}_1\right) \\ \boldsymbol{\tau}_{12}^z\left(\mathbf{P}_2\right) = -\boldsymbol{\tau}_{02}^z\left(\mathbf{P}_2\right).\end{cases} \tag{5}$$

We consider different sizes of commercial permanent magnets for PM0, PM1, and PM2, and vary the actuating distance ratios $\alpha_r = r_{02}/r_{12}$. The angle difference between $\theta_1$ and $\theta_2$ is shown in Fig. 3(b), which grows nonmonotonically with $\theta_0$. Our model indicates that the angle difference is small, which can be reduced to $\sim 1.5^\circ$ by controlling $\mathbf{m}_1$, $\mathbf{m}_2$, and $\alpha_r$. Meanwhile, the actual angle difference can be further reduced by friction, which is validated by experimental data in Section V. Thus, we assume $\theta_1 = \theta_2$ as $\theta_0$ varies, denoted as $\theta$ to represent the rotation of PM1 and PM2. As $\theta_0$ of rotating PM0 varies from 0 to $-2\pi$, $\theta$ increasing from 0 to $2\pi$, and an angle $\theta = \theta_b \in [0, \pi/2)$ is expected when PM1 begins to bounce off, which are valid for both aligning state and magnetic chaining state as $\theta < \theta_b$.

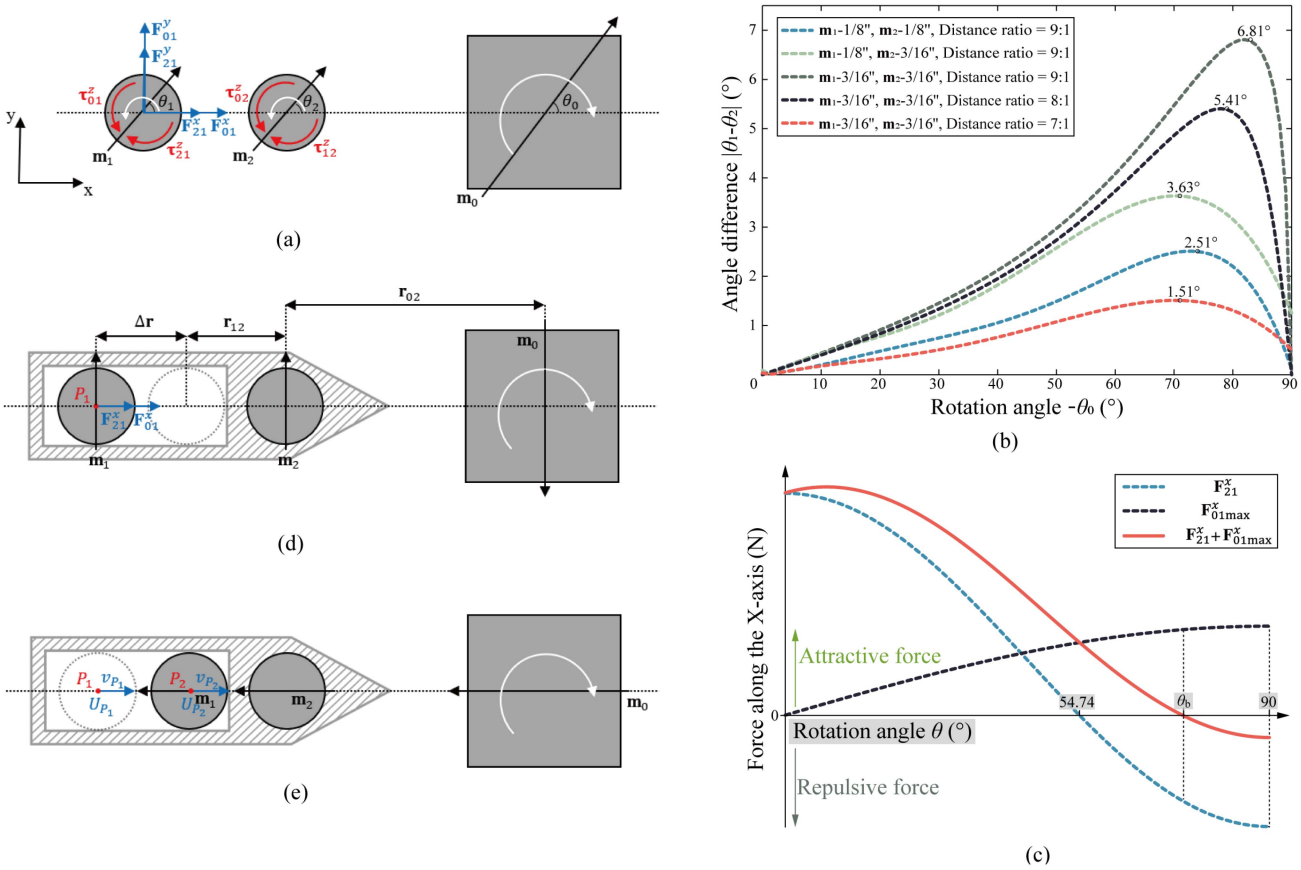


Fig. 3. Angular transformations, positions, and orientations of the magnetic components in different states. (a) A schematic describing the basic parameters involved in the mathematical model of the triple-magnet system. (b) A simulation of the angle differences $|\theta_1 - \theta_2|$ varying with $\theta_0$. The simulating cubic magnet PM0 has a sidelength of two inches and a magnetic moment of 140.317 Am$^2$. The simulated data of magnetic components are collected from commercial NdFeB magnets (K&J Inc.). (c) The magnetic forces exerted by PM0 and PM2 on PM1 vary with $\theta$. (d) A critical bouncing-off state when PM1 bounces off for a maximum distance $\triangle r_{\max}$. (e) An ideal orientation when PM1 hits back, where all the magnetic dipole moments are aligned along the $X$-axis.

### *B. Magnetic Chaining State*

The magnetic forces and torques follow $\propto r_{ij}^{-4}$ and $\propto r_{ij}^{-3}$ based on (2), (3), and (4), respectively. Thus, the local magnetic interaction between PM1 and PM2 is supposed to be strong due to the relatively small $r_{12}$. It can accomplish an even stronger global magnetic interaction by controlling $\mathbf{m}_0$ and $r_{02}$ with PM0. In this case, PM1 and PM2 are attractive to each other attributed to the local interaction. They rotate synchronously due to the global interaction generated by PM0, referred to as magnetic chaining, which is presented in Fig. 2(b).

The torque between PM0 and PM2 mainly determines the angle $\theta$, given the one between PM0 and PM1 is much weaker. The global torque $\tau_{02}^z$ must overcome the internal torque $\tau_{12}^z$ between PM2 and PM1 to ensure synchronized rotation. Based on (4), the internal torque is

$$\tau_{12}^z = -\frac{3\mu_0 m_1 m_2}{8\pi r_{12}^3} \sin 2\theta. \tag{6}$$

To investigate the minimum magnetic torque required to lift PM1 and PM2 from the magnetic chaining state, we consider a critical condition, where the magnetic torque $\tau_{02}^z(\theta_0, \theta)$ is the function of both $\theta_0$ and $\theta$. It is observed from the experiments in Section V that $\theta_0 \sim -\frac{\pi}{2}$ where a maximum torque $\tau_{02\max}^z$ is

$$\tau_{02\max}^z = -\frac{\mu_0 m_0 m_2}{4\pi r_{02}^3} \cos\theta. \tag{7}$$

Thus, to ensure the rotation of PM1 and PM2 in the chaining state, it is required that $|\tau_{02\max}^z| \geq |\tau_{12}^z|$. To simplify the inequality, an estimation is made to remove $\theta$. Thus, we have the sufficient and unnecessary conditions

$$\alpha_r \leq \left(\frac{m_0}{3m_1}\right)^{\frac{1}{3}}. \tag{8}$$

Based on (3), the force exerted by PM2 to PM1 in the $X$-axis is calculated as

$$F_{21}^x = \frac{3\mu_0 m_1 m_2}{4\pi r_{12}^4}\left(2\cos^2\theta - \sin^2\theta\right). \tag{9}$$

Under a rotating magnetic field exerted by PM0, PM1, and PM2 can rotate simultaneously for the same degree $\theta$. As $\theta$ increases up to a critical angle $\theta_m = 54.74°$, $F_{21}^x$ changes from attractive force to repulsive force as shown in Fig. 3(c), which drives the system into the prebouncing state.

### C. Prebouncing State

Due to the global magnetic interaction between PM1 and PM0, the additional attractive force $F_{01}^{x}$ exerted by PM0 to PM1 prevents PM1 from bouncing off immediately. As PM1 and PM2 rotate to $\theta_m = 54.74°$, PM1 is yet to be bounced off, as illustrated in Fig. 2(c). The force $F_{01}^{x}(\theta_0, \theta)$ is maximized with $\theta_0 = -\frac{\pi}{2}$, and thus $F_{01\max}^{x}$ is calculated by (10)

$$F_{01\max}^{x} = -\frac{3\mu_0 m_0 m_1}{4\pi \left(r_{12} + r_{02}\right)^4} \sin\theta. \tag{10}$$

We plot the forces $F_{01\max}^{x}$ and $F_{21}^{x}$ with respect to the chaining angle $\theta$ in Fig. 3(c), and the total force $F_{21}^{x} + F_{01\max}^{x}$ applied to PM1 is calculated. The internal force between PM1 and PM2 changes from attractive to repulsive as $\theta$ increases, while the global force between PM1 and PM0 remains to be attractive and increases with $\theta$. When PM1 is ready to bounce off, it is required that the total force is repulsive. Thus, by solving $F_{21}^{x} + F_{01\max}^{x} = 0$, the lower limit of the distance ratio $\alpha_r$ is obtained

$$\alpha_r \geq \left(\frac{m_0}{m_2}\right)^{\frac{1}{4}} - 1. \tag{11}$$

We note that (11) is the necessary and insufficient conditions of $|F_{21}^{x}| \geq |F_{01\max}^{x}|$, and is also obtained by removing the function of $\theta \in [54.74°, \pi/2)$.

### D. Bouncing-off State

PM1 bounces off along the $X$ direction as the actuating distance ratios $\alpha_r$ fall between the ranges determined by (8) and (11). The corresponding maximum bouncing-off distance of PM1 is denoted as $\triangle r_{\max}$. An ideal state with maximum bouncing-off distance is shown in Fig. 3(d), where all magnetic moments of the triple-magnet system align with the $Y$-axis. Such a configuration is further verified by experiments in Section V. Based on the ideal configuration at point $\mathbf{P}_1$, $\triangle r_{\max}$ is calculated via the force balance $F_{01\max}^{x}(\mathbf{P}_1) = -F_{21}^{x}(\mathbf{P}_1)$

$$\triangle r_{\max} = -\frac{r_{02}\left(\frac{m_2}{m_0}\right)^{\frac{1}{4}}}{\left(\frac{m_2}{m_0}\right)^{\frac{1}{4}} - 1} - r_{12}. \tag{12}$$

### E. Hitting-Back State

As PM0 continues to rotate clockwise, PM1 hits back to the initial position $\mathbf{P}_2$ after achieving the maximum bouncing-off distance $\triangle r_{\max}$. An ideal alignment of the triple-magnet system with maximum impact velocity is illustrated in Fig. 3(e), where all the magnetic moments align along the $X$-axis. During the hitting-back process, the velocity of PM1 at point $\mathbf{P}_1$ is $v_{P_1} = 0$, and the velocity $v_{P_2}$ at point $\mathbf{P}_2$ is calculated based on the conservation of energy

$$U_{P_1} - U_{P_2} = \frac{1}{2}\bar{m}v_{P_2}^2 \tag{13}$$

where $\bar{m}$ is the mass of PM1, $U_{P_j}$ is the magnetic potential energy of PM1 at point $\mathbf{P}_j$, which is calculated by

$$U_{P_j} = -\mathbf{m}_1 \cdot \sum_i \mathbf{B}_i\left(\mathbf{P}_j\right). \tag{14}$$

As PM1 hits the end at the right-hand side, the impact force $F(t)$ is calculated based on the momentum theorem

$$p_c = -\bar{m}v_{P_2} = \int_0^{t_c} F(t)dt \tag{15}$$

where $p_c$ is the momentum for compression and $t_c$ is the impact time. Considering a very small $t_c$ as measured in Section V, we assume the impact force $F(t)$ is independent of time and is denoted as $F$. The force acts on the inner wall and transfers to the robot structure, partially lost as the impact is not perfectly elastic. The loss of kinetic energy is calculated as [32]

$$\Delta E = \frac{1}{2}\bar{m}v_{P_2}^2(1 - e_*^2) \tag{16}$$

where $e_*$ is the kinematic coefficient of restitution. Considering the collision without viscoelastic dissipation, $e_*$ is calculated as

$$e_* = \frac{p_f - p_c}{p_c} \tag{17}$$

where $p_f$ is the terminal impulse for restitution in the robot body illustrated in Fig. 6(b). The restitution coefficient $e_*$ can be measured through a free drop experiment involving a targeted magnetic sphere and impact substrate. Based on the components determined in Section IV, the same NdFeB spherical magnet PM1 as used in the proposed robot is released to the substrate with the same material (PLA) as the 3-D printed external shell. By calculating the ratio of bounce-off height and free drop height, $e_*$ is measured as $0.35 \pm 0.04$. Combining (13) to (17), we obtain the impact force $F$ of the triple-magnet system applied to the environment.

More technical details concerning the needle modeling and the insertion dynamics are discussed in our previous work [33], including needle size optimization, buckling analysis, substrate compression, and contact shear force. The penetration performance is affected by both the needle's geometry (e.g., needle tip, diameter, length) and the substrate's mechanical properties (e.g., Young's modulus). In this work, a stainless-steel clinical needle (25 G, Kindly Medical Inc.) is used as a functional and interchangeable tip of the robot. The needle's modulus is about 200 GPa, six orders higher than most soft tissues in the human body. Therefore, the stiffness difference is less significant in puncture performance, and we focus on the dynamics of the triple-magnet system.

## IV. Optimization of Millirobot

### A. Optimization of Parameters

In this section, we aim to maximize impact force $F$ for the triple-magnet system. According to the mathematical model in Section III, we tune the impact force $F$ with parameters $(m_0, m_1, m_2, r_{12}, r_{02})$, as illustrated in Fig. 4(a).

We consider a uniform magnetization $M$ of commercially available NdFeB magnets, where PM1 and PM2 are N42-graded

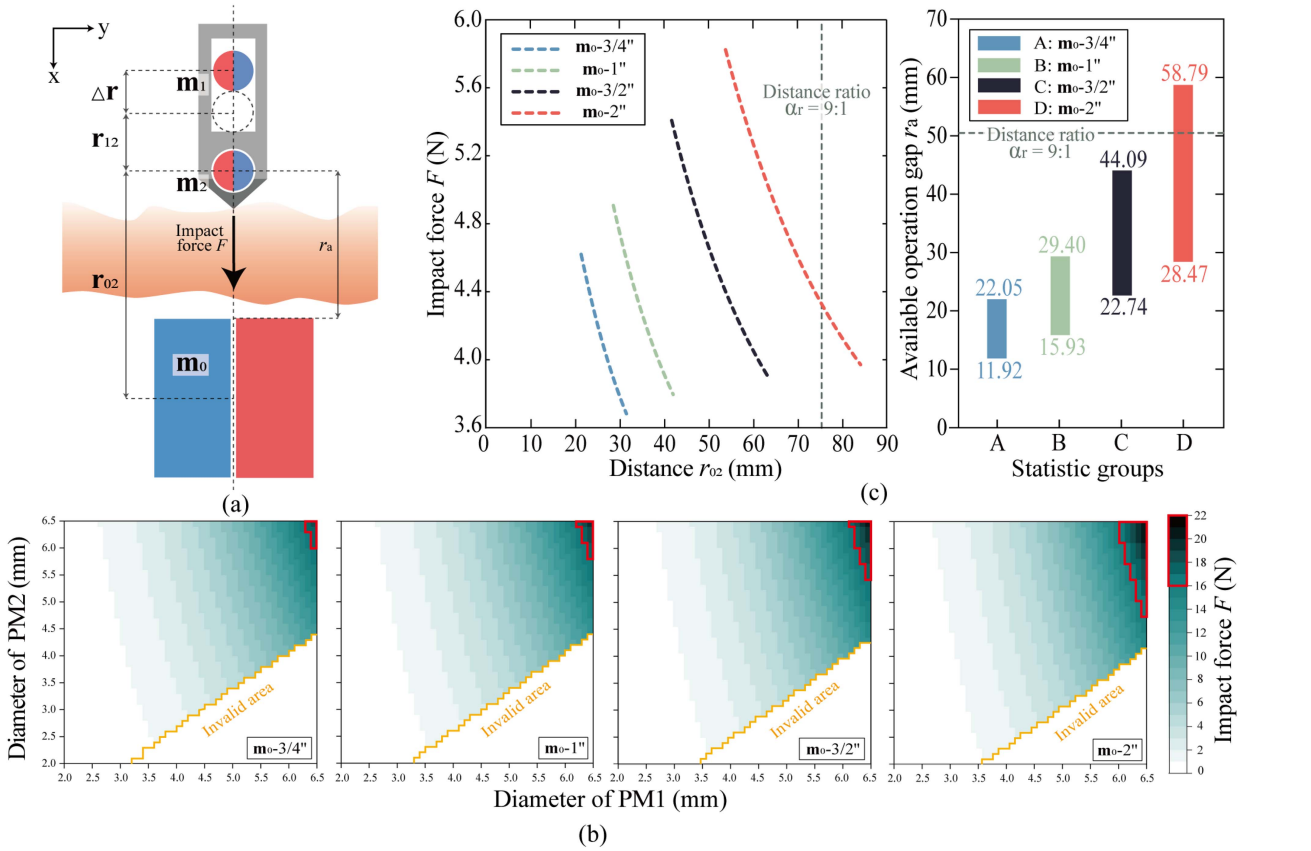


Fig. 4. Parameters optimization for the triple-magnet system. (a) Definitions of the relevant parameters of the triple-magnet system in real-world applications. A specific available operation distance $r_a$ is marked out. (b) 2-D distribution maps illustrating the impact force with varying diameters of PM1 and PM2. Four groups of PM0 with different sidelength values are evaluated. Invalid areas are marked, while impact forces exceeding 16.0 N are highlighted with red color. $r_{12} = 8.4$ mm, distance ratio $\alpha_r$ is the mean value of the upper and lower limits calculated from (8) and (11). (c) Achievable actuating distance ranges and impact forces of different PM0. The actual operation gaps $r_a$ of various PM0 are compared. The diameters of both PM1 and PM2 are 3/16 in, $r_{12} = 8.4$ mm.

(K&J Inc.) spherical magnets, and PM0 is an N52-graded (X-Mag Inc.) cubic magnet. The magnetic moments are calculated as follows:

$$\mathbf{m}_i = \mathbf{M}_i V_i \tag{18}$$

where $\mathbf{M}_i$ is the magnetization, varying with the magnetic grades, and $V_i$ is the volume of the magnetic components. Based on the model presented in Section III, the impact forces with varying diameters of PM1 and PM2 are presented in Fig. 4(b). Both diameters of PM1 and PM2, ranging from 2.0 mm to 6.5 mm, are simulated under the actuation of PM0 with diameters of 3/4 in, 1 in, 3/2 inches, and 2 inches. It is demonstrated that larger diameters in PM1 and PM2 generate a larger impact force, and the effect of the diameter change in PM1 is more significant than that in PM2. In addition, a triangular "Invalid area" with zero impact force is identified, where the PM2 cannot escape from the magnetic chaining state as PM0 rotates. Interestingly, increasing the magnetic moment in PM0 with a larger volume only slightly increases the impact force, and reduces the invalid area of zero impact force. The cubic magnets PM0 produce a similar magnetic gradient at their corresponding available distance range regardless of their volume, resulting in a similar impact force output.

Based on the results from Fig. 4(b), we choose a diameter of 4.76 mm (3/16 in) for both PM1 and PM2 to minimize the angle difference. Meanwhile, we determine a $r_{12} = 8.4$ mm to restrain the size of MINRob and the value of $r_{02}$. It is attributed to the fact that an overly large $r_{12}$ leads to an increase in the general size of the robot and a decrease in the outputting impact force, while an extremely small $r_{02}$ is required to unlock the strong magnetic chaining state between PM1 and PM2 under an overly small $r_{12}$. Therefore, we choose an intermediate quantity $r_{12} = 8.4$ mm, for which an ideal performance of MINRob is also observed in the experiment. In addition, this value is also larger than 3.5 radii of the minimum bounding sphere of both PM1 and PM2, limiting the error from the dipole model.

Although the size of PM0 does not dramatically raise the impact force according to Fig. 4(b), it significantly affects the performance in the manner of an available range of the actuating distance. The distance ratios $\alpha_r$ are calculated through (8) and (11). The corresponding actuating distance $r_{02}$ follows:

$$\left(\left(\frac{m_0}{m_2}\right)^{\frac{1}{4}} - 1\right) r_{12} \leq r_{02} \leq \left(\frac{m_0}{3m_1}\right)^{\frac{1}{3}} r_{12}. \tag{19}$$

TABLE I
ACTUATING DISTANCE $r_{02}$ FOR PM0 WITH DIFFERENT SIDELENGTH

| Sidelength | Magnetic moment $\mathbf{m}_0$ | Minimum $r_{02}$ | Maximum $r_{02}$ |
|---|---|---|---|
| 3/4 in | 8.0596 Am$^2$ | 21.44 mm | 31.57 mm |
| 1 in | 19.1042 Am$^2$ | 28.63 mm | 42.10 mm |
| 3/2 inches | 64.4767 Am$^2$ | 41.79 mm | 63.14 mm |
| 2 inches | 140.3170 Am$^2$ | 53.87 mm | 84.19 mm |

TABLE II
SPECIFICATIONS OF THE TRIPLE-MAGNET SYSTEM

| Symbol | Description | Value |
|---|---|---|
| $m_0$ | Magnetic moment of the actuating cube | 140.3170 Am$^2$ |
| $m_1$ | Magnetic moment of the active sphere | 0.0506 Am$^2$ |
| $m_2$ | Magnetic moment of the passive sphere | 0.0506 Am$^2$ |
| $r_{12}$ | Distance between PM1 and PM2 | 8.4 mm |
| $r_{02}$ | Distance between PM0 and PM2 | 75.6 mm |
| $\alpha_r$ | Distance ratio of $r_{02}$ over $r_{12}$ | 9:1 |
| $l_{\text{chamber}}$ | Length of the inner chamber of MINRob | 8.0 mm |
| $l_{\text{robot}}$ | Total axial length of MINRob | 17.5 mm |
| $d_{\text{robot}}$ | Diameter of MINRob | 5.6 mm |
| $l_{\text{needle}}$ | Length of the needle | 7.0 mm |
| $d_{\text{needle}}$ | Diameter of the needle | 0.5 mm |

The distance ranges of four groups of PM0 are listed in Table I, and the corresponding impact force values are plotted to the left of Fig. 4(c). The transition between chaining state and prebouncing state determines the range of the actuating distance $r_{02}$. The impact force increases with the increase of $\mathbf{m}_0$, and decreases rapidly with the increase of $r_{02}$.

In biomedical applications, the available operation ranges need to be larger than the thickness of the wall of specific skin and organs in human bodies. Considering the volume of PM0, we define the available operation gap $r_a$, which is the gap between MINRob and actuating magnets, marked in the Fig. 4(a). Thus, the available operation distance between the robot and the surface of the actuating magnet is plotted on the right-hand side of Fig. 4(c). In our experiments, we choose an N52-graded magnetic cube with a sidelength of 2 in to ensure the proposed system is applicable for potential in vivo wireless actuation in the future. The corresponding maximum available distance $r_a$ is 58.79 mm, sufficient for operations in abdominal organs [34].

### B. Design Choice of the Magnetic Millirobot

Based on the results of optimization, the fundamental parameters of MINRob and the triple-magnet system are determined and listed in Table II. The values of the magnetic moment are measured by a Gaussmeter (MAGSYS HGM09 s) and calculated in MATLAB via (2). MINRob has a total length of 17.5 mm and a diameter of 5.6 mm. Both spherical magnets PM1 and PM2 are sealed inside the external shell made of PLA as introduced in Section II. Both the inner spherical and cylindrical chambers have a slightly larger diameter (5.1 mm) than the diameter of PM2 and PM1, resulting in free rotation. Meanwhile, the cylindrical chamber with a length of 8 mm allows PM1 to translate reciprocally. We fix a $r_{12} = 8.4$ mm and a $\alpha_r = 9{:}1$ to control the total length of MINRob and ensure safety in experiments. Under such distance values, the N52-graded PM0 (X-Mag Inc.) is able to generate a magnetic field with a magnetic flux density of $\sim 60$ mT at the location of MINRob ($\alpha_r = 9{:}1$, $r_{02} = 75.6$ mm). The N42-graded NdFeB spherical magnet with a diameter of 3/16 in (K&J Inc.) is chosen for both PM1 and PM2. The clinical needle attached to the robot's tip has a total length of 7.0 mm, and $\sim$5.6 mm is exposed outside the robot's body.

## V. CHARACTERIZATION OF TRIPLE-MAGNET SYSTEM

In this section, we verify the applicability of the proposed triple-magnet system, including the five states illustrated in Fig. 2, values of specific critical angles analyzed in Section III, and the available range of actuating distances measured by (19). In addition, more factors (i.e., impact time, the rotation frequency of PM0, and the real-time hitting-back angle of PM0), which have yet to be discussed in our model, are experimentally evaluated.

### A. Angle Variations of Triple-Magnet System

First, the various states during a completed impact process and the corresponding critical angles of each magnetic component are investigated. To this end, a customized experimental setup with details introduced in Fig. 6(a) in Section V-B, is employed using a high-speed optical camera (MotionBLITZ mini2, Mikrotron GmbH) to obtain real-time imaging illustrating the position and orientation of each magnetic component in the triple-magnet system. PM1 and PM2 are encapsulated in a 3-D printed frame, while PM0 is rotating on the right side. A metal spray paint is applied to the south pole of PM1 and PM2 with black dyeing, and thus the direction of the magnetic moment is visualized during the rotation. The images are obtained at a frame rate of 1000 fps and rotation frequencies of PM0 range from 0.25 to 3.0 Hz.

Representative curves for the angle variations of PM1 and PM2 in a complete rotation period at 0.5 Hz are presented in Fig. 5. The angle data are presented as the mean measured value with a sample size of 5. The real-time rotation angles of PM1 and PM2 are denoted as $\theta_1$ and $\theta_2$, respectively. During the magnetic chaining and prebouncing state, the curves for both $\theta_1$ and $\theta_2$ are the same. The peak angle difference is $|\theta_1 - \theta_2| = 2.31^\circ$, verifying the assumptions of $\theta_1 = \theta_2$ in the mathematical model in Section III. As PM1 starts to bounce off and further hit back, the angle difference increases as the local interactions between PM1 and PM2 weaken. In the bouncing-off and hitting-back state, the impact process is measured with the energy in (14) and (15), where a large angle difference is observed. Eventually, $\theta_1$ and $\theta_2$ approach each other and increase simultaneously to $\pi$ in an aligning manner, as illustrated in Fig. 5.

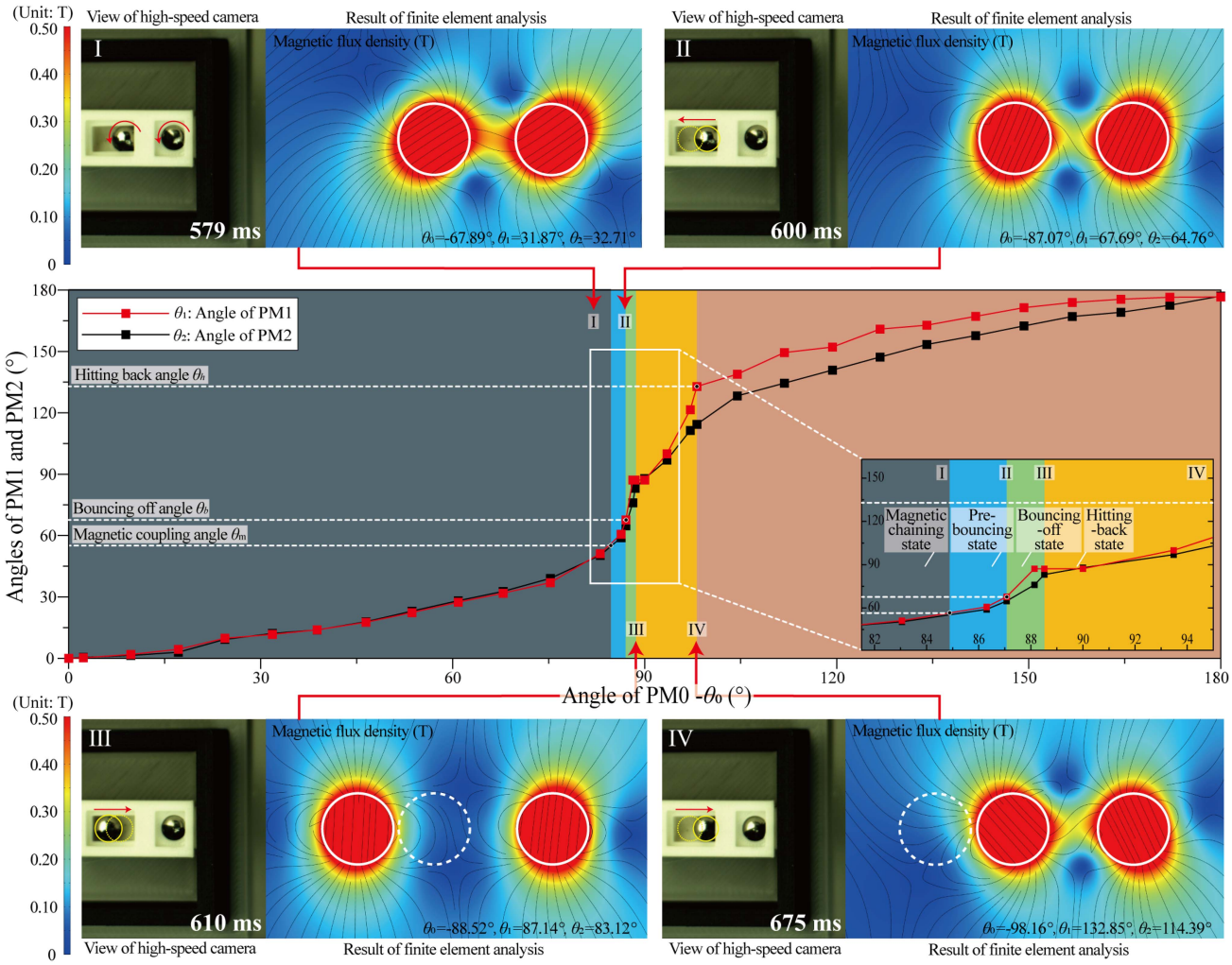


Fig. 5. Representative curves illustrating angle variations of PM1 and PM2. The data are obtained by the high-speed camera in a complete rotation period at a rotation frequency of 0.5 Hz. The mean angle values are presented in the figure with a sample size of 5, while specific angles are marked out. Snapshots of the specific transitional states are listed together with corresponding FEA results illustrating the magnetic flux density distribution. I: Transitional states between magnetic chaining state and prebouncing state; II: Transitional states between prebouncing state and bouncing-off state; III: Transitional states between bouncing-off state and hitting-back state; IV: The ending moment of the hitting-back state.

The proposed five states (i.e., aligning state, magnetic chaining state, prebouncing state, bouncing-off state, and hitting-back state) are observed in experiments. They are illustrated in the figure with different background colors. Specific critical angles of transitions between states are marked out, for which the real-time images illustrating the position and orientation of PM1 and PM2 are presented in the figure. For a rotation frequency of 0.5 Hz, the duration of 21 ms, 10 ms, and 65 ms are recorded for the prebouncing state, bouncing-off state, and hitting-back state, respectively.

Correspondingly, an FEA is demonstrated in COMSOL Multiphysics 5.5 for magnetic flux density distribution of the triple-magnet system in a complete rotation period, as presented in Supplementary Video I. A specific configuration $[\theta_0, \theta_1, \theta_2] = [-67.89°, 31.87°, 32.71°]$ is illustrated for magnetic chaining state. The region of interest (ROI) between PM1 and PM2 presents a strong connection with a high magnetic flux density. The magnetic chaining state is reached in a configuration of $[\theta_{m\_0}, \theta_{m\_1}, \theta_{m\_2}] = [-84.90°, 56.05°, 53.74°]$, where the magnetic flux density of the ROI decreases as $|\theta_0|$ increases. As a critical configuration $[\theta_{b\_0}, \theta_{b\_1}, \theta_{b\_2}] = [-87.07°, 67.69°, 64.76°]$ is accomplished during the prebouncing state, a low magnetic flux density of the ROI results in the magnetic repulsive force between PM1 and PM2, leading to the bouncing-off in PM1. A maximum bouncing-off distance $\triangle r_{\max}$ is observed during the bouncing-off state in a configuration $[\theta_0, \theta_1, \theta_2] = [-88.52°, 87.14°, 83.12°]$. Eventually, PM1 hits back in a configuration $[\theta_0^*, \theta_{h\_1}, \theta_{h\_2}] = [-98.16°, 132.85°, 114.39°]$.

### B. Setup and Distance Evaluation

Here, we aim to measure the force generated by the proposed triple-magnet system and collect real-time images simultaneously. In our experimental setups, it is infeasible to directly place the force sensor between the actuating magnet and the robot. The

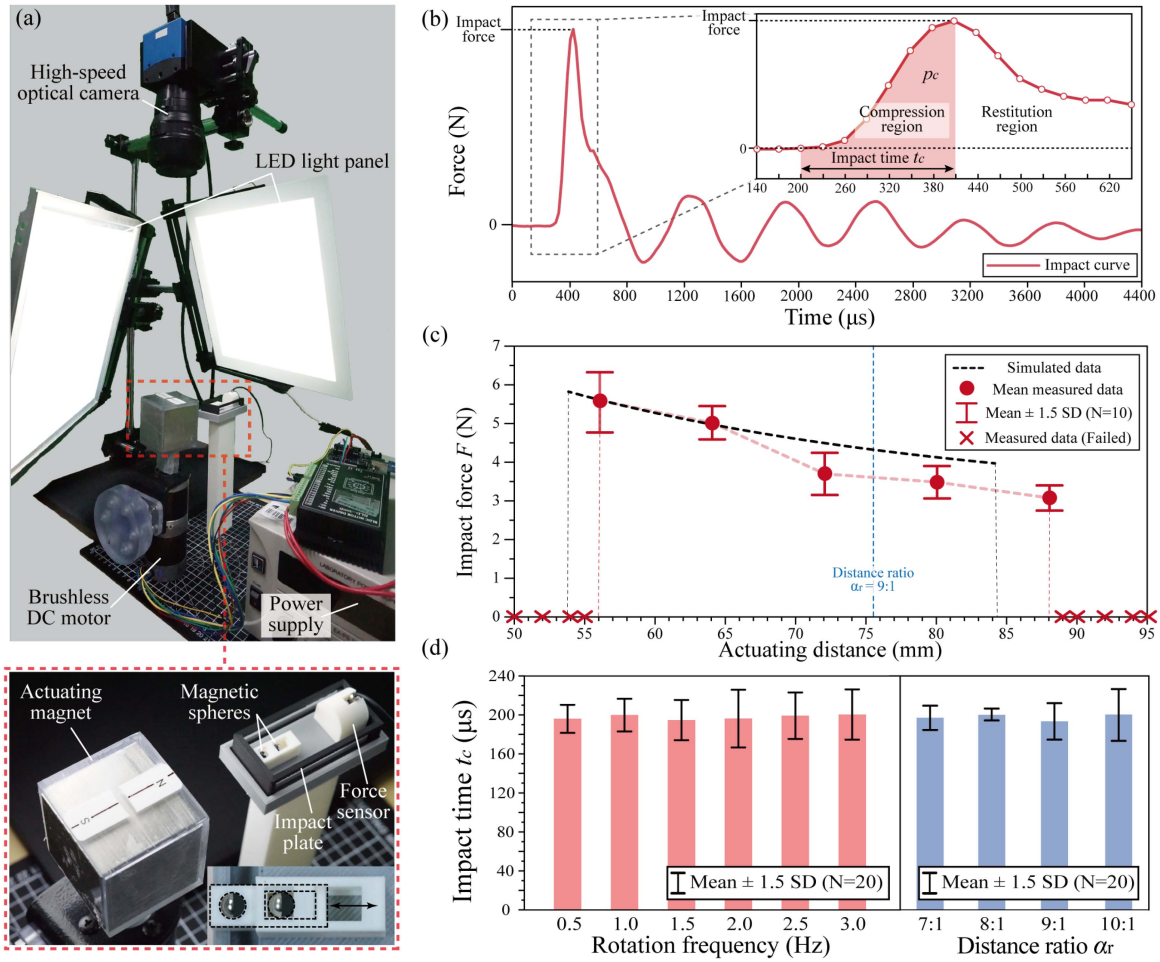


Fig. 6. Experimental setup and results of the evaluation of the impact process. (a) Images of the experimental setup. The impact plate is 3-D printed via carbon fiber reinforced ABS and is placed inside a groove with WD-40 lubricant to reduce friction. (b) A representative measured impact force profile. A one-time impact curve is composed of the compression region and restitution region. The compression region is marked in red color and is considered the impact region, while the differences of $X$ and $Y$ coordinates are time $t$ and impact force $F$, respectively. (c) Impact force with varying actuating distances. The force values and available actuating distance ranges are presented and compared with the simulated data. The red cross stands for the actuating distance, where the triple-magnet system is not able to operate, i.e., PM1 cannot bounce off. Error bar represents $\pm 1.5$ standard deviations (SD), sample size (N) $= 10$. (d) Left: Impact time $t_c$ varies with the rotation frequency of the motor. Distance ratio $\alpha_r = 9:1$. Right: Impact time $t_c$ varies with distance ratio $\alpha_r$. Rotation frequency $= 0.5$ Hz. Error bar represents $\pm 1.5$ SD, sample size (N) $= 20$.

force sensor will collide with the rotating magnet, and the strong time-varying magnetic field induces an undesired perturbation in measurements. To avoid the aforementioned issues, we design a customized experimental setup to measure the impact force indirectly, as shown in Fig. 6(a). A piezoelectric force sensor (DYTRAN 1051V1, 10 LbF) with a nonmagnetic impact cap and a data acquisition module (DEWSOFT IOLITEi-1×ACC, 50 kHz) is placed sufficiently far from the rotating magnet. The impact force from the robot is transmitted to the sensor via a 3-D printed rigid impact plate composed of carbon fiber reinforced acrylonitrile butadiene styrene (ABS), which is lightweight with ideal impact property [35], [36]. Two spherical magnets, PM1 and PM2 are enclosed in a structure similar to MINRob. They are positioned in a plastic frame, allowing the structure to hit the impact plate to mimic the impact process of MINRob. The impact experiments have the same parameters as the triple-magnet system, as defined in Table II.

A representative impact force curve is illustrated in Fig. 6(b). To measure the impact force at different actuating distances, we further apply external support to fix the PM1 at the distal end first, holding a bouncing-off state before releasing PM1 as PM0 rotates to the ideal configuration, as described in Fig. 3(e). The results are presented in Fig. 6(c), where the impact force output decreases as the actuating distance increases. Meanwhile, the available actuating distance $r_{02} \in [56, 88]$ (mm) is experimentally demonstrated, where PM1 bounces off with the rotation of PM0. The impact forces in experiments are comparable to the model predictions in Fig. 4(c), and an actuating distance $r_{02} \in [53.87, 84.19]$ (mm) predicted by Table I also matches well with experiments.

### C. Investigation of Rotation Frequency

The rotation frequencies of the actuating magnet (PM0) also affect the impact process. We investigate its effect by measuring

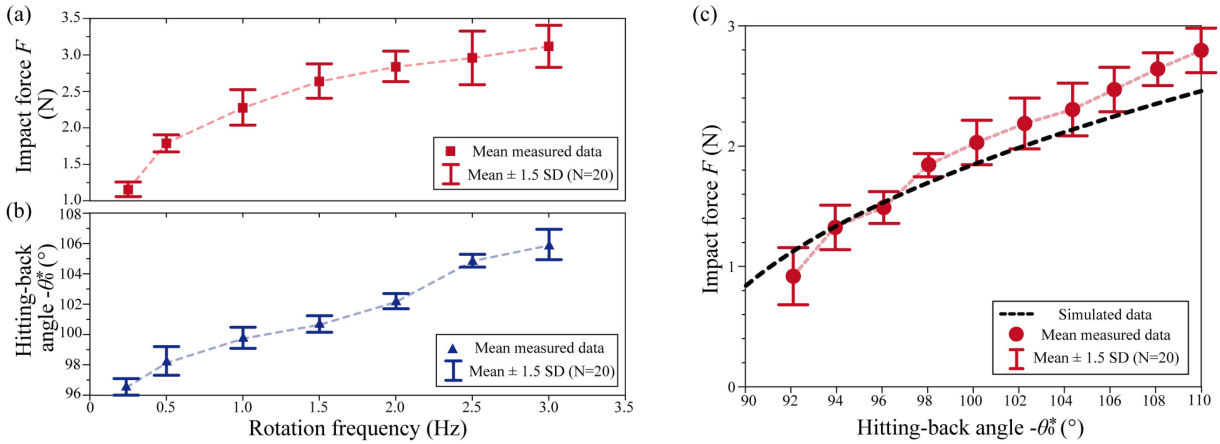


Fig. 7. Experimental data of characterization of the impact process. (a) Impact force $F$ with varying rotation frequency of the actuating permanent magnet PM0. (b) Hitting-back angle $\theta_0^*$ with varying rotation frequency of the actuating permanent magnet PM0. A similar trend is observed matching with data from (a). (c) Impact force $F$ with varying hitting-back angle PM0 of the actuating permanent magnet PM0, the experimental data are compared with the simulated data. Error bar represents ±1.5 SD, sample size (N) = 20.

the evolution of impact force over time in experiments. As presented in Fig. 6(b), the collision between the active spherical magnet PM1 and the robot body is divided into the compression and restitution phases. In the compression phase, the kinetic energy of PM1 is transformed into the elastic energy of the contact surface and dissipation energy. Afterward, the elastic energy is released during the restitution phase. Herein, the impact time $t_c$ is defined as the duration of the compression phase, while impact force $F$ is the peak force value [32]. Experiments showed that the impact time $t_c$ is not significantly affected by rotation frequency (Fig. 6(d)). In addition, an approximately constant impact time $t_c = 200\ \mu$s is observed in the triple-magnet system for different distance ratios $\alpha_r$. It is noted that an impact time $t_c = 400\ \mu$s has been reported in impact between a magnetic part and a glass mica ceramic contact surface [22].

Although different rotation frequencies result in a constant impact time $t_c = 200\ \mu$s, they still affect the impact force. As illustrated in Fig. 7(a), $F$ increases with increasing rotation frequency from 0.25 Hz to 3.0 Hz. PM1 is static for a certain period at the proximal end after each impact. Thus the dynamic effect (e.g., kinetic energy accumulation after each impact) from the continuously rotating magnetic field is negligible.

During the impact experiment, PM1 has already hit back before PM0 rotates to an ideal configuration where $\theta_0 = -\pi$ as illustrated in Fig. 3(e). Since both the bouncing-off and hitting-back time of PM1 are much shorter than the period of the rotation of the actuating magnet. Thus, we have

$$|\theta_0^*| < \pi \tag{20}$$

where $\theta_0^*$ is the rotating angle of PM0 at the instant PM1 hits back. We further evaluate the hitting-back angle $\theta_0^*$ at different rotation frequencies of the motor, as shown in Fig. 7(b). The angle data are obtained via a high-speed optical camera, and the detailed information is introduced in the following subsection. As the rotation frequency rises from 0.25 to 3.0 Hz, $|\theta_0^*|$ increases from 96.54° to 105.86°. Our results implied that a higher rotation frequency allows the PM0 to rotate for a larger $|\theta_0^*|$, getting closer to the ideal configuration of $|\theta_0^*| = \pi$ in Fig. 3(e), and thus the increment of impact force output is observed.

In summary, it is experimentally suggested that the rotation frequency of the actuating magnets affects the impact forces of the triple-magnet system. Instead of changing the impact time $t_c$, it changes the hitting-back angle $\theta_0^*$, and the subsequent impact process. Although the impact force increases with the rotation frequency, it is suggested that by manipulating such a large permanent magnet with a robotic arm, the rotation frequency should not exceed 0.5 Hz [11], [12]. Thus, we choose 0.5 Hz as the standard rotation frequency for the actuating magnets to balance force and safety. Further tuning the angle $\theta_0^*$ during the hitting-back process to achieve better performance is beyond the scope of the current study.

In addition, we estimate the hitting-back angle $\theta_0^*$ based on our mathematical model. For an ideal state presented in Fig. 3(e), both attractive forces $F^x_{01\max}$ and $F^x_{21\max}$ exerted on PM1 contribute to the acceleration during the hitting-back process. The components in the $X$-axis of these attractive forces are maximized because all magnetic dipole moments of PM0, PM1, and PM2 align with each other along the $X$-axis. If PM1 hits back as described in (20), the attractive force from PM0 has a $Y$ component, resulting in an undesired swing, and the rest of the attractive force in the $X$-axis is calculated as

$$F^x_{01} = F_{01\max} \cos\theta_0^*. \tag{21}$$

Hence, as $\theta_0^* \to -\pi$, $F^x_{01}$ is maximized. This alignment for PM0 in the $X$ component contributes to a larger magnetic potential energy of PM1 as described in (13) due to the potential energy induced simultaneously by PM0 and PM2

$$U_{P_j} = -\mathbf{m}_1 \cdot \sum_{i=0,2} \mathbf{B}_i(\mathbf{P}_j) = -\mathbf{m}_1 \cdot (\mathbf{B}_0(\mathbf{P}_j) + \mathbf{B}_2(\mathbf{P}_j)) \tag{22}$$

where $\mathbf{B}_0(\mathbf{P}_j)$ and $\mathbf{B}_2(\mathbf{P}_j)$ is the magnetic flux density at point $P_j$ generated by PM0 and PM2, respectively. When $\theta_0^* = -\pi$,

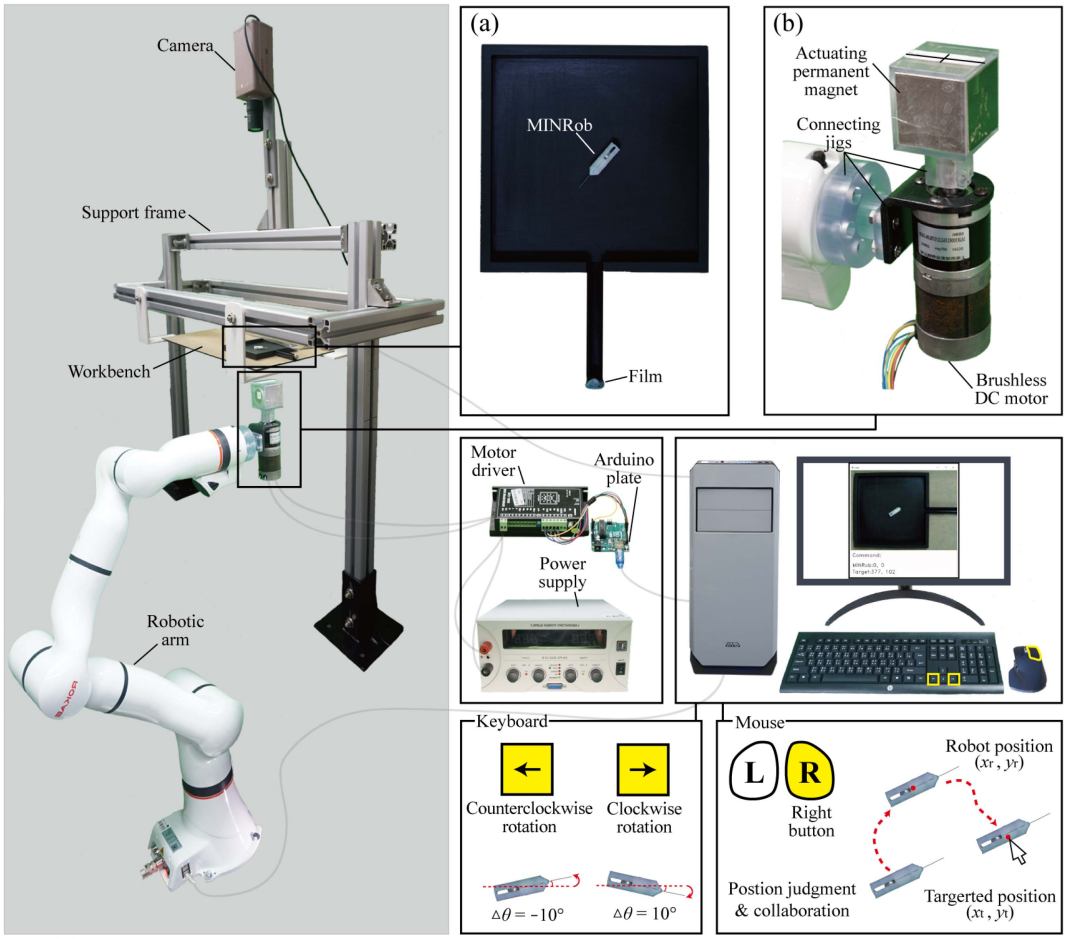


Fig. 8. Schematic illustrating the teleoperation robotic system controlled by the keyboard and mouse. (a) The 3-D printed workbench and MINRob. The workbench is composed of a rectangular 2-D plane and a hollow tube. (b) The connection among PM0, motor, and the robotic arm.

$|\mathbf{m}_1 \cdot \mathbf{B}_2(\mathbf{P}_2)|$ is maximized, and thus a maximum impact force $F$ is achieved by (13), (14), and (15).

The influence of various $\theta_0^*$ to the impact force $F$ is experimentally investigated through the setup in Fig. 6(a). In the initial configuration, the active spherical magnet PM1 is fixed by the external support to its bouncing-off state. When the actuating permanent magnet PM0 rotates to a specific angle $\theta_0^*$, the external support is removed, and the impact force values are recorded. The experimental data is presented in Fig. 7(c) and compared with the simulated data measured by (21). Here, $-\theta_0^* \in [90°, 110°]$ is evaluated, which is the achievable range of the present peripheral via tuning the rotation frequency. It is experimentally proved that a larger hitting-back angle $|\theta_0^*|$ of the triple-magnet system generates a larger impact force.

## VI. Locomotion and Functionality

### A. Teleoperated Locomotion Demonstrations

We introduce a triple-magnet teleoperation robotic system to create a remotely controllable and programmable magnetic field, as illustrated in Fig. 8. We manipulate the actuating permanent magnet PM0 and collect optical images simultaneously. The system comprises the MINRob, the actuating permanent magnet PM0, a brushless dc motor, a seven-DOFs robotic arm, an optical camera, and a personal computer (PC).

A customized workbench composed of a rectangular 2-D plane and a hollow tube with a multilayer film attached to its end is fabricated, as shown in Fig. 8(a). The locomotion and penetration performance of MINRob is demonstrated in the 2-D plane and the tube, respectively.

A commercially available cubic permanent magnet (N52-graded NdFeB, X-Mag Inc.) with a sidelength of 2 inches is chosen as the actuating magnet PM0. Its rotation is controlled via a brushless dc motor by tuning its rotation frequency and orientation. The brushless dc motor has a maximum no-load rotation speed of 307 r/min and a rated torque of around 4.63 Nm. PM0 is concentrically connected with the rotation axis of the motor via a 3-D printed mold. Together with the motor, the actuating magnet is attached to the tip of a seven-DOFs robotic arm (ROKAE xMate ER7 Pro) using an aluminum frame and a 3-D printed base. By adjusting the parameters of each joint, the orientation and position of PM0 can be accurately controlled. Due to a limit of the maximum rotation angle of each joint in the robotic arm, the rotation of the actuating magnet is mainly controlled by the brushless dc motor. The state, direction, and rotation frequency can be programmed in an Arduino circuit

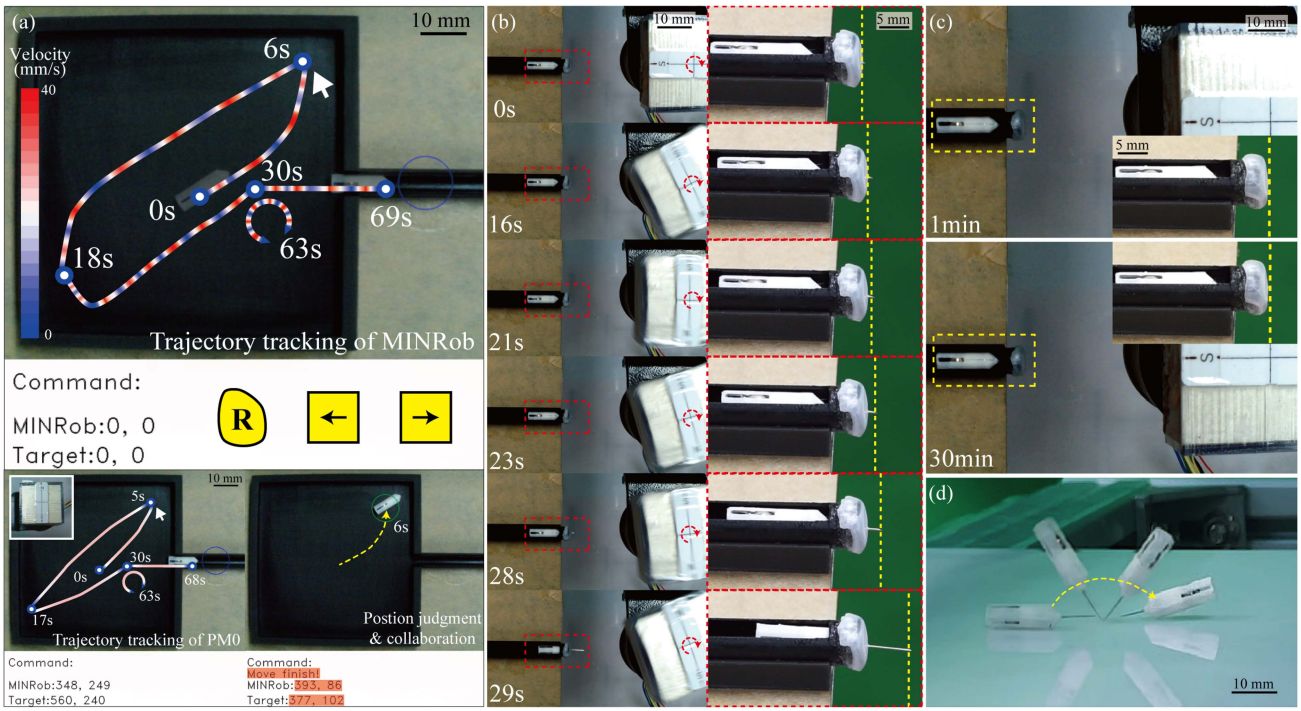


Fig. 9. Experimental demonstrations of the locomotion and puncturing capabilities of the proposed small-scale robot. (a) The planar locomotions of the MINRob integrated with the teleoperation robotic system. By clicking via the mouse, the MINRob is able to reach the targeted position, while a controllable rotation is accomplished by pressing the keyboard. The real-time trajectories of both MINRob and PM0 are illustrated with their velocities presented by various colors, sharing the same color scale. A position judgment and collaboration process is demonstrated. (b) The penetration performance of the MINRob to puncture a multilayer film. The film is completely punctured under the impact induced by the triple-magnet system within 30 s. (c) A control group for the penetration performance. The pure magnetic attractive force fails to puncture the film for more than 30 min. (d) A 3-D rolling motion of the MINRob. A forth and back rolling is achieved under the rotation of the actuating permanent magnet in the lateral direction.

plate and controlled by a PC. Here, the actuating permanent magnet PM0 and the motor are shown in Fig. 8(b), and the orientation of the PM0 is fixed. By controlling the translation of PM0 via the robotic arm (approximately 12 cm beneath the workbench), the MINRob will navigate on the planar surface.

Furthermore, an optical camera and Open Source Computer Vision library are employed to record the outline of the MINRob and obtain its position and orientation. By connecting to the PC, a customized C$^{++}$ program controls the position and orientation of the MINRob remotely. The user can use the mouse to provide a targeted position $P_t^c \in \mathbb{R}^{2\times1}$ in the frame of the camera $O^c(x_c, y_c)$ by clicking the right button in the operation interface, where the real-time images are provided by the camera. Afterward, $P_t^c$ is transferred into position $P_t^w \in \mathbb{R}^{2\times1}$ in the frame of the workbench $O^w(x_w, y_w)$ by translating the digital pixel from the user interface to the real-world dimension of the workbench. Finally, position $P_t^w$ is transferred into $P_t^r \in \mathbb{R}^{2\times1}$ in the frame of the robotic arm $O^r(x_r, y_r)$ based on the relative position between the workbench and the end tip of the robotic arm. The robotic arm locates the PM0 to the targeted point $P_t^r$, and the MINRob is navigated to the targeted position $P_t^w$ in the workbench.

A position judgment and collaboration procedure is introduced to evaluate the translation's precision. The coordinates of both robot and the targeted point are displayed during the translation. If the mismatch of the targeted position and terminal robot position is smaller than one body length of the MINRob, the moving is considered a successful process and displays the text: "Move finish!". Otherwise, a collaboration procedure is implemented, where PM0 moves vertically away from the workbench and returns to the initial position to restart the movement.

To adjust the orientation of the MINRob, the robotic arm rotates the PM0 to exert a magnetic torque, forcing the MINRob to align with its magnetic moment through rotation. By pressing the "←" ("→") button on the keyboard, PM0 rotates counterclockwise (clockwise) along the $Z$-axis, resulting in the same rotation of the MINRob, and enables the orientation control of MINRob.

The demonstration of planar locomotion is presented in Fig. 9(a) and Supplementary Video II. The command interface shows the real-time coordinate of the robot's position while displaying the coordinate of the targeted position after each click via mouse. The MINRob successfully moves to the targeted positions in the rectangular plane with a distance mismatch less than one body length. The trajectory of MINRob is presented with each targeted point and timing being marked out. Afterward, the MINRob is rotated to be aligned with the axial direction of the hollow tube by pressing the "←" and "→" buttons on the keyboard. Ultimately, the MINRob is driven into the hollow tube after a total time of 69 s. As shown in Supplementary Video II, the translational motion of MINRob is not completely smooth in the response of the translation of PM0. It is attributed to the

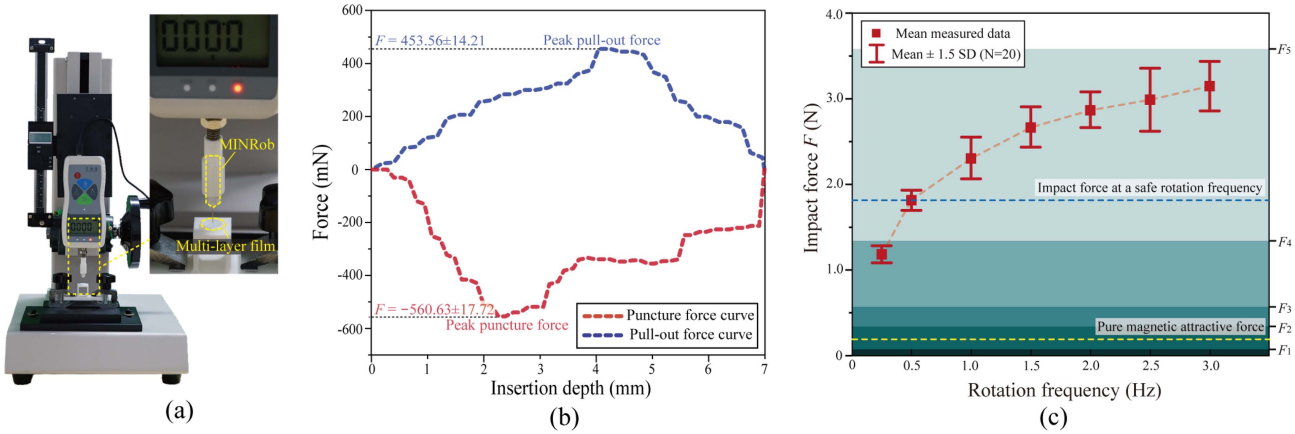


Fig. 10. Experimental setup and results of the penetration evaluation. (a) An experimental setup mimicking the impact process. A digital force gauge is attached to a spiral test rack, which provides a controllable displacement to the MINRob. The multilayer film is fixed on a jig, and thus the puncture force and the pull-out force are measured during a complete insertion and extraction process, respectively. (b) The representative curves of both puncture and pull-out forces vary with the insertion depth. The peak force values represent the mean value ± 1.5 SD, with the sample size being 24. (c) A comparison of the force value between the proposed triple-magnet system and specific application scenarios. Its outputting force values are adjustable to meet the requirements of various tissue penetrations, for which the specific force values are listed in Table III.

TABLE III
SPECIFICATIONS OF THE PARAMETERS IN FIG. 10(C)

| Symbol | Description | Value [Ref.] |
|---|---|---|
| $F_1$ | Puncture force for mouse brain | 2.50 mN [37] |
| $F_2$ | Puncture force for human cornea | 282 mN [38] |
| $F_3$ | Puncture force for piglet skin | 0.54 N [39] |
| $F_4$ | Puncture force for porcine tissue | 1.28 N [40] |
| $F_5$ | Puncture force for piglet skin (blunted needle) | 3.54 N [39] |

friction caused by the gradient pulling. The geometric shape of the MINRob prevents an ideal rolling motion in any direction. To illustrate this intricate dynamic motion, the real-time trajectory of MINROb is demonstrated in lines with various colors denoting the velocity at each position by processing the video frame. MINRob tends to leap during its translation, thus, blue regions represent the pause positions during each clicking. In comparison, we present the trajectory tracking of PM0 with its velocity variation. Although MINRob didn't follow PM0's path perfectly, it is experimentally suggested that all standstill points for MINRob and PM0 matched well.

In summary, the planar locomotions of the MINRob, including the translation and rotation performance, are demonstrated with a teleoperation robotic system. Such a system accomplishes the remotely programmable and precise manipulation of the proposed MINRob, indicating a potential application to be integrated with the advanced robot-assisted operation system. In addition, a 3-D rolling locomotion is achieved by rotating PM0 in the lateral plane, as illustrated in Fig. 9(d). Rolling motion without net displacement, forth rolling, and back rolling are presented in Supplementary Video III.

### B. Penetration Demonstrations

The performance of the triple-magnet system to generate a larger force is evaluated by the penetration experiment. To provide structural support, a hollow tube is connected to the workbench with an inner diameter of 6 mm, slightly larger than the MINRob. A multilayer laboratory film (Parafilm M), which is composed of a blend of waxes and polyolefins, is attached at the distal end. A single layer of the film has a thickness of 127 $\mu$m, we use five layers in total to mimic the multilayer structure of the muscle. In addition, the laboratory film demonstrates a promising stretchability of over 200% of its original length at breaking, which is comparable to some muscle tissues [41]. After the MINRob is navigated into the hollow tube, the actuating permanent magnet PM0 further pulls the MINRob to the distal end. Afterward, PM0 is located to a targeted position by the robotic arm and starts to rotate at a safe frequency of 0.5 Hz, as presented in Supplementary Video IV.

As shown in Fig. 9(b), the triple-magnet system actuates the repeatable impact due to the rotation of PM0, which generates a continuous force output. The clinical needle attached to the MINRob tip can puncture five layers of film within 30 s. The bouncing-off and hitting-back procedures of the PM1 are observed, while an obvious puncture is observed from the needle tip after each impact, verifying the applicability of the proposed triple-magnet system in the real device. The corresponding control group is shown in Fig. 9(c), where PM0 is placed in the same position while the magnetic dipole moment is aligned with the axial direction of the MINRob to induce a pure magnetic attractive force. It is observed that MINRob is not able to puncture the multilayer film in such a configuration for more than 30 min, indicating the pure magnetic attractive force is insufficient to penetrate the film at the same condition.

### C. Characterizations of Puncture

To quantitatively evaluate the penetration performance, a digital force gauge (HANDPI, 10 N, 0.01%) is employed to measure the puncture force and the pull-out force of the MINRob, as shown in Fig. 10(a). The robot body is encapsulated by a 3-D printed casing connected to the force gauge, while the

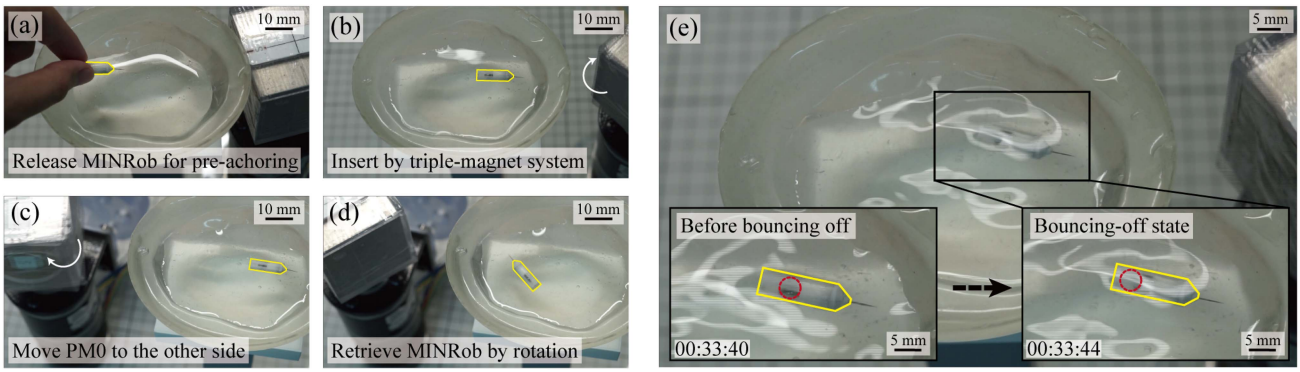


Fig. 11. Insertion of MINRob in a 3-D unconstrained environment. (a) PM0 is positioned in the vicinity of the wall of the PDMS mold. A small part of the needle tip is able to anchor on the inner wall when MINRob is released. (b) PM0 is actuated by the motor and rotated at 1.0 Hz on the right side of the PDMS mold. Thus, a continuous insertion of the needle is achieved by the impact induced by the triple-magnet system. (c) PM0 is moved to the left side of the PDMS mold after insertion. (d) MINRob is pulled out and retrieved under the rotation of PM0 on the other side. (e) A screenshot of a bouncing-off motion.

force gauge is fixed on a spiral test rack which can provide a precise and controllable displacement in the vertical direction. By providing a similar approaching speed for the MINRob as measured from the experiment, the force curve is measured for both the penetration and pull-out process. Representative curves for puncture and pull-out forces with increasing penetration depth are illustrated in Fig. 10(b). A peak puncture force of –560.63±17.72 mN is measured, while a peak pull-out force is 453.56±14.21 mN. It is noted that the pure magnetic attractive force in Fig. 9(c) is measured to be 171.13 mN based on (3). The corresponding impact force for the triple-magnet system with a 0.5 Hz rotation frequency is measured to be 1.81 N, indicating a ten-fold increase. Thus, the triple-magnet system is able to provide a significantly larger outputting force compared with a pure magnetic pulling force. It is capable of being applied for tissue penetration while providing substantial anchoring.

The proposed MINRob is able to provide continuous outputting forces ranging from 1.17 to 2.92 N under various rotation frequencies (from 0.25 to 3.0 Hz). These values are illustrated in Fig. 10(c) while comparing to specific force thresholds in biomedical applications, and the corresponding force parameters are listed in Table III. Compared to the conventional magnetic miniature robots driven by attractive magnetic force (171.13 mN) with the same characteristic length, our triple-magnet system provides a force output with a tenfold increase. For a rotation frequency of 0.5 Hz, an impact force of 1.81 N is accomplished, which is sufficient for penetrating the mouse brain, human cornea, piglet skin, and porcine tissue.

### *D. Insertion in a 3-D Unconstrained Environment*

To extend the application scope of our proposed system, we present the on-demand insertion of MINRob in a 3-D unconstrained environment. First, we customize a bowl-like 3-D structure composed of soft elastomer. Polydimethylsiloxane (PDMS) is chosen with a mass ratio of 20:1 (silicone base to the curing agent) while its shear modulus is measured as ∼150 kPa via a uniaxial tensile test. This value is comparable to the one of skeletal muscle tissues [42]. The mixture of silicon base and curing agent is poured into a customized 3-D printed mold, and cured for 48 h at room temperature after vacuuming. The PDMS mold with a semiellipsoid shell shape is molded from a bladder phantom. The lengths of semiaxes of the inner semiellipsoid are $a = 31$ mm, $b = 42$ mm, and $c = 40$ mm, while the average thickness of the shell is around 12.8 mm.

Previous demonstration in Fig. 9(b) is constrained in a 1-D impact. To accomplish a 3-D insertion, preanchoring is required as structural support to stabilize the orientation of MINRob and avoid the synchronous rotation with PM0. As illustrated in Fig. 11(a), the anchoring is achieved by manually releasing MINRob in the vicinity of the PM0, which is positioned close to the targeted insertion point on the PDMS mold. During the experiment, the PDMS mold is filled with water to mimic the potential application scenarios involving fluidic filling (e.g., body fluids and blood). PM0 enables a fast approach for MINRob along the direction of its magnetic moment and results in inserting a small part of the needle tip.

Afterward, PM0 is moved away from the PDMS mold to ensure an available gap based on (19) to actuate the triple-magnet system for impact with a rotation frequency of 1.0 Hz. In the beginning, the needle tip's limited insertion depth results in continuous swinging on the robot body. The swing amplitude reduces dramatically with the increasing insertion depth. Eventually, the needle is inserted deeper at an operating time period of ∼291 s, as shown in Fig. 11(b).

In real-world applications, removing our robot after conducting specific tasks is critical. Thus, we move PM0 to the other side of the PDMS mold after insertion, as presented in Fig. 11(c). Afterward, PM0 is rotated similarly to exert both magnetic force and torque to pull MINRob out. In Fig. 11(d), the needle continues to slide out until the robot is completely unanchored within ∼15 s.

In such a case, both on-demand insertion and retrieval of MINRob in an unconstrained 3-D environment are achieved, as recorded in Supplementary Video V. We plotted the real-time insertion depth for the preanchoring, insertion, and retrieval processes in Fig. 12. The clinical needle is dyed black, and a red line marks out the contact horizontal plane between the needle

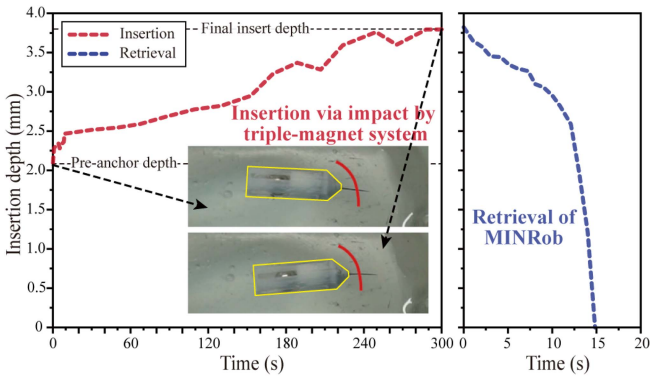


Fig. 12. Real-time insertion depth of the needle tip during both insertion and retrieval procedures. The insertion depth refers to the distance between the needle tip and the surface of the PMDS mold. Left: Insertion depth with varying operation time during the insertion process. Right: Insertion depth with varying operation time during the retrieval process.

and the PDMS mold. The needle has a total length of 7.0 mm, and ∼5.6 mm is exposed outside the robot's body. Finally, the needle with a depth of 2.06 mm is inserted after preanchoring, while an insertion depth of 3.82 mm is eventually accomplished via the triple-magnet system. In Fig. 11(e), a screenshot from the video is captured to illustrate a successful bouncing-off motion, validating the feasibility of the triple-magnet system in an unconstrained 3-D environment.

## VII. Discussion

In the previous sections, the reliability of the proposed triple-magnet system is verified by mathematical modeling and experimental demonstrations. Based on this, the MINRob is designed. Under an externally rotating permanent magnet, the MINRob is able to achieve reversible and continuous collision along any direction in 3-D space, supported by the structural to MINRob.

Although a comprehensive study of MINRob is demonstrated, more factors influencing the robot's locomotion have yet to be discussed. Among them, friction is a critical parameter. We experimentally investigate the impact forces under various friction by utilizing the same setup as introduced in Fig. 6(a). It is suggested that the decrease of friction is not able to increase the impact force significantly. Similar results are obtained from estimating the friction values. There are two types of friction during the demonstration of MINRob in the manner of translation, rotation, and insertion. A contact happens between the robot and a solid boundary, which is referred to as external friction. In addition, we discuss the internal friction that happens between the inner magnetic sphere PM1 and the internal wall of the PLA shell. By measuring the coefficients of both external and internal friction, and the weight of each component in MINRob, the internal sliding friction and external sliding friction are estimated to be $2.88 \times 10^{-4}$ N and $9.00 \times 10^{-4}$ N, respectively. These values are several orders of magnitude smaller compared to the magnetic force ($\sim 10^{-1}$ N) and impact force ($\sim 10^{0}$ N). Therefore, when the MINRob is actuated in a manner of insertion via the rotating PM0, both internal and external friction can hardly affect the performance and the force output of the proposed triple-magnet system.

It is noted that we also demonstrated the locomotion of the MINRob in a manner of translation and rotation, for which PM0 is placed beneath the robot integrated with the teleoperation system, as shown in Figs. 8 and 9(a). In this case, the component of a similar magnetic attractive force ($\sim 10^{-1}$ N) in the $Z$-axis generated from PM0 to MINRob also contributes to the friction. As PM0 moves away from MINRob, the component of the magnetic attractive force in the $Z$-axis decreases, resulting in a drop of static friction on the external surface. When the component of the magnetic attractive force in $XY$-plane is larger than the decreasing static friction, MINRob suddenly leaps from its original position to the current position of PM0. Therefore, the translation locomotion of MINRob presented in Fig. 9(a) is not as smooth as expected.

In addition to friction, there are other possible factors that affect the performance of our triple-magnet system. First, we investigate the contribution of gravity in the manner of energy. As the triple-magnet system changes between the state illustrated in Fig. 3(d) and (e), the center of mass shifts reciprocally and results in a variation in gravitational potential energy. This variation of the potential energy in the axial direction of MINRob is measured as $\sim 10^{-5}$ J, which is much smaller compared with the magnetic potential energy ($\sim 10^{-2}$ J). Although the effect from the shifting center of mass is negligible for the impact process considering the potential energy, gravity itself influences the puncture performance of MINRob. It is experimentally observed that the insertion is challenging when the gravity is opposite to the direction of impact. In the meantime, the influence of the filling fluid inside the PDMS mold remains to be studied. In the real-world biomedical scenario, the body fluids or the blood result in a different locomotion pattern compared to the water we used due to various viscosity and Reynolds numbers.

To apply our system to real-world biomedical applications, several technical issues need to be considered. To deliver the MINRob through narrow spaces and reach the deep-buried targeted lesion, the robot's size should be limited. The current design demonstrates a robot structure with a total length of ∼23 mm and a diameter of 5.6 mm, which is compatible with the scale of clinical capsules (e.g., 000 capsule). In addition, the biocompatibility of currently utilized materials is to be investigated. PLA shell of the MINRob is highly biocompatible with tissues, while a biodegradable needle [18], [47] can replace the current needle and enhance the reliability for long-term anchoring. The previous section demonstrated penetration control in an unconstrained 3-D environment under sufficient visual information. Considering a limited visualization in a real clinical scenario, position feedback is required (e.g., optical images obtained from ultrasound imaging). Furthermore, an appropriate actuating distance is demanded as described in (19). By estimating the approximate value of the wall thickness of the targeted organ or the distance from the inner wall to the skin surface, the position and orientation of the magnet can be precisely controlled to effectively trigger the triple-magnet system.

Finally, we present a comparison of this work with the current miniature magnetic robots in Table IV. We compared our work

TABLE IV
COMPARISON OF THE OUTPUTTING FORCE OF MINIATURE MAGNETIC ROBOTS WITH VARIOUS WORKING PRINCIPLES

| Characteristic length | Robot shape | Field generator | Working principle | Repeatable operation | Force output | Ref. |
|---|---|---|---|---|---|---|
| 2.7 mm | Needle | Electromagnetic coils | Magnetic force and torque | Yes | 0.23 mN | [31] |
| 3.2 mm | Needle | Radio frequency heater | Releasing pre-stored elastic energy via a spring | No | 0.95 N | [18] |
| 10.8 mm | Scissor | Radio frequency heater | Releasing elastic energy via pre-stretched coiled muscle | No | $\sim$ 2 N | [17] |
| 15.0 mm | Scissor | Electromagnetic coils | Magnetic torque | Yes | 35 mN | [43] |
| 17.5 mm | Needle | Permanent magnet | Momentum-based impact (two magnetic parts) | Yes | 1.81 N | This work |
| 21.0 mm | Gripper | Electromagnetic coils | Magnetic torque | Yes | 6 mN | [44] |
| 22.0 mm | Needle (capsule) | Electromagnetic coils | Magnetic force and torque | Yes | 0.60 N | [45] |
| 35.4 mm | Needle | Electromagnetic coils | Momentum-based impact (magnetic and nonmagnetic parts) | Yes | 0.41 N | [22] |
| 40.0 mm | Capsule | Permanent magnet | Magnetic force | Yes | 0.60 N | [46] |
| 100 mm | Hammer | Electromagnetic coils | Momentum-based impact (magnetic and nonmagnetic parts) | No | $\sim$ 0.59 N | [19] |

with previous research reporting magnetic robots with similar characteristic lengths, geometric shapes, or working principles. It is suggested that additional energy obtained from either preprocessing structures or momentum-based impact is beneficial for a larger force output, although a few designs are triggered by bulky and sophisticated field generators (e.g., radio frequency heaters and electromagnets). Previous small-scale robots cannot simultaneously accomplish a sufficient force output and continuous operation while maintaining a small size. The triple-magnet system introduced here achieves a significantly large force output accompanied by a repeatable operation. In addition, its force output is adjustable by controlling the rotation frequency of PM0, for which we can constrain the force output of MINRob to protect the tissue from being penetrated in specific surgical situations.

In vivo tissue penetration demonstrates great significance in medical applications. The drug delivery efficiency of administration routes is limited by various biological barriers (e.g., gastrointestinal mucus barriers and bladder penetrating barriers [48]). Treatments of specific diseases require breaking through these barriers and accessing the deep muscle layer (e.g., muscle-invasive bladder cancer [49]). However, in vivo tissue penetration via a wireless robot poses a great challenge to current robot design due to the scaling law. The proposed MINRob and triple-magnet system demonstrate great potential to access deep tissue and conduct operations (e.g., tissue biopsy and drug delivery), inspiring the development of small-scale robots that are more applicable to tissue penetration. Our robot has the potential to treat muscle-invasive bladder cancer in a minimally invasive manner. The small diameter allows MINRob to be delivered through a clinical urinary catheter, while the retrieval process is proceeded by rotating PM0 at another side of the bladder penetration. MINRob is able to puncture the needle to the deep bladder muscle and prevent perforation at the same time. By integrating with specific functional units, our proposed system demonstrates promising potential in various in vivo applications in minimally invasive healthcare. For example, customized microsensors [50] and flexible electronics [51] inside the MINRob are able to conduct implant therapy for long-time monitoring. Loading with specific drugs [18], [47], MINRob potentially enables drug delivery on the targeted bladder muscle layer. In addition, this triple-magnet system is potentially capable of a highly precise ex vivo insertion (e.g., acupuncture [52]) under the teleoperation system at an even longer distance [53].

## VIII. CONCLUSION

In this article, we propose a novel triple-magnet system, which enables a reversible and repeatable magnetic collision between two spherical magnets. The proposed mechanism is verified by mathematical modeling and experiments. To extend the application of the triple-magnet system, a miniature device MINRob, is introduced based on the magnetic impact to exert large force via a needle, integrating with a teleoperation system. Eventually, experimental demonstrations are presented to evaluate the locomotion and penetration performance of the MINRob. We compare the output force and the achievable force range between our work and the current miniature magnetic robots, indicating the potential applications of the triple-magnet system in tissue penetration.

Although we have significantly raised the ceiling of magnetic force by impact, even better performance is achievable. The current system cannot achieve an ideal configuration during the hitting-back state due to the restraints from the peripheral, leading to the loss of impact force. Meanwhile, the insertion efficiency of the needle is limited due to the inevitable swinging motion on the MINRob's body under the rotating PM0. Therefore, the potential developments and future optimizations are needed, which include additional mechanisms to delay the hitting-back process and outer encapsulations to reduce undesired swinging. Spring and glues are available alternatives to raise the hitting-back force threshold while reducing the impact energy loss. An outer encapsulator [54] is able to prevent the needle from penetrating into a nontarget area. In addition, adhesive films [55] can be integrated into the encapsulator's surface, which fixes the robot at the targeted surface while leaving the needle out to perform the penetration. With these potential developments, the side-effect of the swinging can be reduced, and thus higher insertion efficiency and reliability can be achieved.

## ACKNOWLEDGMENT

The authors would like to thank Songnan Bai (City University of Hong Kong) for the technical support of the high-speed camera, Yi Zheng (City University of Hong Kong) for fruitful discussions, and Luohui Zhou (Harbin Institute of Technology, Shenzhen) for suggestions about revision.

## REFERENCES

[1] Y. Wang, J. Shen, S. Handschuh-Wang, M. Qiu, S. Du, and B. Wang, "Microrobots for targeted delivery and therapy in digestive system," *ACS Nano*, vol. 17, no. 1, pp. 27–50, 2022.

[2] K. E. Peyer, L. Zhang, and B. J. Nelson, "Bio-inspired magnetic swimming microrobots for biomedical applications," *Nanoscale*, vol. 5, no. 4, pp. 1259–1272, 2013.

[3] B. J. Nelson, I. K. Kaliakatsos, and J. J. Abbott, "Microrobots for minimally invasive medicine," *Annu. Rev. Biomed. Eng.*, vol. 12, pp. 55–85, 2010.

[4] T. Gwisai, N. Mirkhani, M. G. Christiansen, T. T. Nguyen, V. Ling, and S. Schuerle, "Magnetic torque–driven living microrobots for increased tumor infiltration," *Sci. Robot.*, vol. 7, no. 71, 2022, Art. no. eabo0665.

[5] V. Magdanz et al., "Ironsperm: Sperm-templated soft magnetic microrobots," *Sci. Adv.*, vol. 6, no. 28, 2020, Art. no. eaba5855.

[6] J. Yu, D. Jin, K.-F. Chan, Q. Wang, K. Yuan, and L. Zhang, "Active generation and magnetic actuation of microrobotic swarms in bio-fluids," *Nature Commun.*, vol. 10, no. 1, 2019, Art. no. 5631.

[7] G. Ciuti, P. Valdastri, A. Menciassi, and P. Dario, "Robotic magnetic steering and locomotion of capsule endoscope for diagnostic and surgical endoluminal procedures," *Robotica*, vol. 28, no. 2, pp. 199–207, 2010.

[8] X. Yang et al., "An agglutinate magnetic spray transforms inanimate objects into millirobots for biomedical applications," *Sci. Robot.*, vol. 5, no. 48, 2020, Art. no. eabc8191.

[9] B. Wang et al., "Endoscopy-assisted magnetic navigation of biohybrid soft microrobots with rapid endoluminal delivery and imaging," *Sci. Robot.*, vol. 6, no. 52, 2021, Art. no. eabd2813.

[10] Q. Ze et al., "Spinning-enabled wireless amphibious origami millirobot," *Nature Commun.*, vol. 13, no. 1, 2022, Art. no. 3118.

[11] T. Wang et al., "Adaptive wireless millirobotic locomotion into distal vasculature," *Nature Commun.*, vol. 13, no. 1, pp. 1–17, 2022.

[12] Y. Kim et al., "Telerobotic neurovascular interventions with magnetic manipulation," *Sci. Robot.*, vol. 7, no. 65, 2022, Art. no. eabg9907.

[13] I. S. Khalil et al., "Magnetic localization and control of helical robots for clearing superficial blood clots," *APL Bioeng.*, vol. 3, no. 2, 2019.

[14] Y. Xiang and J. Zhang, "A theoretical investigation of the ability of magnetic miniature robots to exert forces and torques for biomedical functionalities," *IEEE Robot. Automat. Lett.*, vol. 8, no. 3, pp. 1771–1777, Mar. 2023.

[15] D. Li, M. Jeong, E. Oren, T. Yu, and T. Qiu, "A helical microrobot with an optimized propeller-shape for propulsion in viscoelastic biological media," *Robotics*, vol. 8, no. 4, 2019, Art. no. 87.

[16] S. Park, B. Ko, H. Lee, and H. So, "Rapid manufacturing of micro-drilling devices using fff-type 3D printing technology," *Sci. Rep.*, vol. 11, no. 1, pp. 1–9, 2021.

[17] M. Li, Y. Tang, R. H. Soon, B. Dong, W. Hu, and M. Sitti, "Miniature coiled artificial muscle for wireless soft medical devices," *Sci. Adv.*, vol. 8, no. 10, 2022, Art. no. eabm5616.

[18] R. H. Soon et al., "On-demand anchoring of wireless soft miniature robots on soft surfaces," *Proc. Nat. Acad. Sci.*, vol. 119, no. 34, 2022, Art. no. e2207767119.

[19] J. Leclerc, A. Ramakrishnan, N. V. Tsekos, and A. T. Becker, "Magnetic hammer actuation for tissue penetration using a millirobot," *IEEE Robot. Automat. Lett.*, vol. 3, no. 1, pp. 403–410, Jan. 2018.

[20] A. Quelin, L. Petit, C. Prelle, and N. Damay, "Experimental performance analysis of an electromagnetic impact-drive microrobot," in *Proc. IEEE Int. Conf. Mechatronics*, 2021, pp. 1–6.

[21] J. Zhang, J. Tian, D. Zhu, Y. Liu, and S. Prasad, "Design and experimental investigation of a vibro-impact self-propelled capsule robot with orientation control," in *Proc. Int. Conf. Robot. Automat.*, 2022, pp. 11381–11387.

[22] O. Erin et al., "Overcoming the force limitations of magnetic robotic surgery: Magnetic pulse actuated collisions for tissue-penetrating-needle for tetherless interventions," *Adv. Intell. Syst.*, vol. 4, no. 6, 2022, Art. no. 2200072.

[23] W. Li and G. Wang, "Chiral magnetic effects in nuclear collisions," *Annu. Rev. Nucl. Part. Sci.*, vol. 70, pp. 293–321, 2020.

[24] V. Skokov, A. Y. Illarionov, and V. Toneev, "Estimate of the magnetic field strength in heavy-ion collisions," *Int. J. Modern Phys. A*, vol. 24, no. 31, pp. 5925–5932, 2009.

[25] A. T. Becker, O. Felfoul, and P. E. Dupont, "Toward tissue penetration by mri-powered millirobots using a self-assembled Gauss gun," in *Proc. IEEE Int. Conf. Robot. Automat.*, 2015, pp. 1184–1189.

[26] M. von Strauss und Torney, S. Dell-Kuster, H. Hoffmann, U. von Holzen, D. Oertli, and R. Rosenthal, "Microcomplications in laparoscopic cholecystectomy: Impact on duration of surgery and costs," *Surg. Endoscopy*, vol. 30, pp. 2512–2522, 2016.

[27] M. Salehizadeh and E. Diller, "Three-dimensional independent control of multiple magnetic microrobots via inter-agent forces," *Int. J. Robot. Res.*, vol. 39, no. 12, pp. 1377–1396, 2020.

[28] X. Liang, H. Fu, and A. J. Crosby, "Phase-transforming metamaterial with magnetic interactions," *Proc. Nat. Acad. Sci.*, vol. 119, no. 1, 2022, Art. no. e2118161119.

[29] H. Gu et al., "Self-folding soft-robotic chains with reconfigurable shapes and functionalities," *Nature Commun.*, vol. 14, no. 1, 2023, Art. no. 1263.

[30] A. J. Petruska and J. J. Abbott, "Optimal permanent-magnet geometries for dipole field approximation," *IEEE Trans. Magn.*, vol. 49, no. 2, pp. 811–819, Feb. 2013.

[31] M. P. Kummer, J. J. Abbott, B. E. Kratochvil, R. Borer, A. Sengul, and B. J. Nelson, "Octomag: An electromagnetic system for 5-DoF wireless micromanipulation," *IEEE Trans. Robot.*, vol. 26, no. 6, pp. 1006–1017, Dec. 2010.

[32] W. J. Stronge, *Impact Mechanics*. Cambridge, U.K.: Cambridge Univ. Press, 2018.

[33] H. Quan, X. Liang, X. Zhang, M. A. Meyers, R. M. McMeeking, and E. Arzt, "The shape of Nature's stingers revealed," *Proc. Nat. Acad. Sci.*, vol. 121, no. 7, 2024, Art. no. e2316320121.

[34] A. Costa-Ferreira, P. Rodrigues-Pereira, M. Rebelo, L. O. Vásconez, and J. Amarante, "Morphometric study (macroscopic and microscopic) of the lower abdominal wall," *Plast. Reconstructive Surg.*, vol. 134, no. 6, pp. 1313–1322, 2014.

[35] M. Lay, N. L. N. Thajudin, Z. A. A. Hamid, A. Rusli, M. K. Abdullah, and R. K. Shuib, "Comparison of physical and mechanical properties of PLA, ABS and nylon 6 fabricated using fused deposition modeling and injection molding," *Composites Part B: Eng.*, vol. 176, 2019, Art. no. 107341.

[36] M. Dawoud, I. Taha, and S. J. Ebeid, "Mechanical behaviour of abs: An experimental study using FDM and injection moulding techniques," *J. Manuf. Processes*, vol. 21, pp. 39–45, 2016.

[37] A. A. Sharp, A. M. Ortega, D. Restrepo, D. Curran-Everett, and K. Gall, "In vivo penetration mechanics and mechanical properties of mouse brain tissue at micrometer scales," *IEEE Trans. Biomed. Eng.*, vol. 56, no. 1, pp. 45–53, Jan. 2009.

[38] A. Matthews, C. Hutnik, K. Hill, T. Newson, T. Chan, and G. Campbell, "Indentation and needle insertion properties of the human eye," *Eye*, vol. 28, no. 7, pp. 880–887, 2014.

[39] K. Owen, N. Blackie, and T. J. Gibson, "The effect of needle reuse on piglet skin puncture force," *Vet. Sci.*, vol. 9, no. 2, 2022, Art. no. 90.

[40] M. Khadem, C. Rossa, R. S. Sloboda, N. Usmani, and M. Tavakoli, "Mechanics of tissue cutting during needle insertion in biological tissue," *IEEE Robot. Automat. Lett.*, vol. 1, no. 2, pp. 800–807, Jul. 2016.

[41] C. H. Weppler and S. P. Magnusson, "Increasing muscle extensibility: A matter of increasing length or modifying sensation?," *Phys. Ther.*, vol. 90, no. 3, pp. 438–449, 2010.

[42] C. D. Kuthe and R. V. Uddanwadiker, "Investigation of effect of fiber orientation on mechanical behavior of skeletal muscle," *J. Appl. Biomaterials Funct. Mater.*, vol. 14, no. 2, pp. 154–162, 2016.

[43] O. Onaizah and E. Diller, "Tetherless mobile micro-surgical scissors using magnetic actuation," in *Proc. Int. Conf. Robot. Automat.*, 2019, pp. 894–899.

[44] C. Forbrigger et al., "Cable-less, magnetically driven forceps for minimally invasive surgery," *IEEE Robot. Automat. Lett.*, vol. 4, no. 2, pp. 1202–1207, Apr. 2019.

[45] D. Son, H. Gilbert, and M. Sitti, "Magnetically actuated soft capsule endoscope for fine-needle biopsy," *Soft Robot.*, vol. 7, no. 1, pp. 10–21, 2020.

[46] S. Yim and M. Sitti, "Design and rolling locomotion of a magnetically actuated soft capsule endoscope," *IEEE Trans. Robot.*, vol. 28, no. 1, pp. 183–194, Feb. 2012.

[47] A. Abramson et al., "An ingestible self-orienting system for oral delivery of macromolecules," *Science*, vol. 363, no. 6427, pp. 611–615, 2019.

[48] S. Wang, S. Jin, Q. Shu, and S. Wu, "Strategies to get drugs across bladder penetrating barriers for improving bladder cancer therapy," *Pharmaceutics*, vol. 13, no. 2, 2021, Art. no. 166.

[49] V. G. Patel, W. K. Oh, and M. D. Galsky, "Treatment of muscle-invasive and advanced bladder cancer in 2020," *CA: A Cancer J. Clinicians*, vol. 70, no. 5, pp. 404–423, 2020.
[50] E. Mohagheghian et al., "Quantifying stiffness and forces of tumor colonies and embryos using a magnetic microrobot," *Sci. Robot.*, vol. 8, no. 74, 2023, Art. no. eadc9800.
[51] Y. Xu et al., "In-ear integrated sensor array for the continuous monitoring of brain activity and of lactate in sweat," *Nature Biomed. Eng.*, vol. 7, no. 10, pp. 1307–1320, 2023.
[52] J. Su, Y. Zhu, and M. Zhu, "Hand-eye-force coordination of acupuncture robot," *IEEE Access*, vol. 7, pp. 82154–82161, 2019.
[53] J. Lee, X. Zhang, C. H. Park, and M. J. Kim, "Real-time teleoperation of magnetic force-driven microrobots with 3D haptic force feedback for micro-navigation and micro-transportation," *IEEE Robot. Automat. Lett.*, vol. 6, no. 2, pp. 1769–1776, Apr. 2021.
[54] A. Abramson et al., "A luminal unfolding microneedle injector for oral delivery of macromolecules," *Nature Med.*, vol. 25, no. 10, pp. 1512–1518, 2019.
[55] Z. Chen et al., "A magnetic multi-layer soft robot for on-demand targeted adhesion," *Nature Commun.*, vol. 15, no. 1, Art. no. 644, 2024.

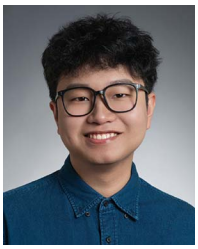

**Yuxuan Xiang** (Graduate Student Member, IEEE) received the B.E. degree in mechanical engineering from Xi'an Jiaotong University (Special Class for the Gifted Young), Xi'an, China, in 2020. He is currently working toward the Ph.D. degree in biomedical engineering with the City University of Hong Kong, Hong Kong.

His research interests include magnetic robots and small-scale robots for minimally invasive surgeries.

**Ruomao Liu** (Student Member, IEEE) received the B.S. degree in biotechnology from Shenzhen University, Shenzhen, China, in 2021, and the M.S. degree in biomedical engineering, in 2022, from the City University of Hong Kong, Hing Kong, where he is currently working toward the Ph.D. degree in biomedical engineering with the Biorobot Laboratory.

His main research interests are in soft robotics and magnetic control.

**Zihan Wei** (Student Member, IEEE) received the M.S. degree in materials science and engineering from Beihang University, Beijing, China, in 2018. He is currently working toward the Ph.D. degree in biomedical engineering with the City University of Hong Kong, Hong Kong.

His research interests include magnetic robots, small-scale robots, and medical robots.

**Xinliang Wang** (Student Member, IEEE) received the B.Eng. degree in aircraft design and engineering and M.Eng. degree in flight vehicle design from Northwestern Polytechnical University, Xi'an, China, in 2019 and 2022, respectively. He is currently working toward the Ph.D. degree in biomedical engineering with the City University of Hong Kong, Hong Kong.

His research interests include magnetic robots, soft continuum robots, and miniaturized robots.

**Weida Kang** received the B.E. degree in engineering mechanics from the Wuhan University of Technology, Wuhan, China, in 2018, and the M.E. degree in mechanics from the Harbin Institute of Technology, Shenzhen, China, in 2021. He is currently working toward the Ph.D. degree in mechanical engineering with the Harbin Institute of Technology, Shenzhen.

His main research interests include constitutive theory of soft materials and mechanical metamaterials.

**Min Wang** (Graduate Student Member, IEEE) received the B.S. degree in mechanical design and manufacturing and automation from the Hefei University of Technology (HFUT), Hefei, China, in 2017, and the M.S. degree in mechanical engineering from the Harbin Institute of Technology Shenzhen (HITSZ), Shenzhen, China, in 2020. He is currently working toward the Ph.D. degree in mechanical engineering with the City University of Hong Kong, Hong Kong.

His main research interests include actuation and perception for miniature robots.

**Jun Liu** (Member, IEEE) received the Ph.D. degree in mechanical and industrial engineering from the University of Toronto, Toronto, ON, Canada, in 2016.

From 2017 to 2019, he was a Postdoctoral Fellow with Weill Cornell Medical College, Cornell University, Ithaca, NY, USA. He is currently an Assistant Professor with the Department of Mechanical Engineering, City University of Hong Kong, Hong Kong. His current research interests include micro–nanorobotics, medical robotics, and smart sensors and actuators.

Dr. Liu was the recipient of multiple awards in the field of robotics and automation including the Best Student Paper Award and the Best Medical Robotics Paper Finalist Award from the IEEE INTERNATIONAL CONFERENCE ON ROBOTICS AND AUTOMATION in 2014, and IEEE TRANSACTIONS ON AUTOMATION SCIENCE AND ENGINEERING Best New Application Paper Award in 2018.

**Xudong Liang** received the bachelor's degree in theoretical and applied mechanics from Sun Yat-Sen University, Guangzhou, China, in 2010, the master's degree in engineering mechanics from Tsinghua University, Beijing, China, in 2013, and the Ph.D. degree in mechanical engineering from the University of California, San Diego, CA, USA, in 2018.

He was a Postdoctoral Researcher with the University of Massachusetts, Amherst, MA, USA, and an Assistant Professor with the Department of Mechanical Engineering, State University of New York at Binghamton, Binghamton, NY, USA. He is currently a Professor with the School of Science, Harbin Institute of Technology, Shenzhen, China. His current research interests include mechanics of soft materials, soft robots, and bionics.

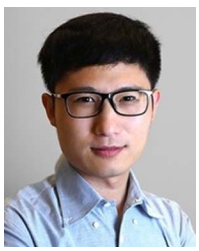

**Jiachen Zhang** (Member, IEEE) received the Ph.D. degree in mechanical and industrial engineering from the University of Toronto, Toronto, ON, USA, in 2018.

He became a Postdoctoral Researcher with the Department of Physical Intelligence, Max Planck Institute for Intelligent Systems, Stuttgart, Germany. In 2021, he became an Assistant Professor with the Department of Biomedical Engineering, City University of Hong Kong (CityU), Hong Kong. His research interests include small-scale medical robotics for minimally invasive diagnostic and therapeutic tasks.